Thesis for the degree of Doctor of Engineering

Local Structure and Dynamics of Next Generation Electrolytes

- linking microscopic and macroscopic properties

FILIPPA LUNDIN

Department of Physics
Chalmers University of Technology
Göteborg, Sweden 2022

Local Structure and Dynamics of Next Generation Electrolytes
- linking microscopic and macroscopic properties
FILIPPA LUNDIN
ISBN: 978-91-7905-688-9

Doktorsavhandlingar vid Chalmers tekniska högskola
Ny serie nr 5154
ISSN 0346-718X.

Department of Physics
Chalmers University of Technology
SE-412 96 Gothenburg
Sweden
Telephone +46 (0)31-772 1000

Cover illustration by Linnéa Rydh

Chalmers, Chalmers digitaltryck
Gothenburg, Sweden 2022

Local Structure and Dynamics of Next Generation Electrolytes
- linking microscopic and macroscopic properties

FILIPPA LUNDIN
Department of Physics
Chalmers University of Technology

Abstract

The electrolyte is a crucial part of a battery in terms of performance, longevity and safety. However, the state-of-the-art electrolytes for lithium-ion batteries are based on organic solvents and Li-salts (typically at 1M concentration) which are volatile and degrade at higher temperatures. In addition, these electrolytes are not suitable for next generation battery concepts where the use of metallic lithium at the anode side is a prerequisite. Thus, there is currently a strong effort to find new electrolyte concepts to both improve safety of current battery technology and pave way for next generation batteries. In the search for new electrolytes, highly concentrated electrolytes and ionic liquids have been proposed as alternatives through properties such as high thermal stability, lower reactivity with cell components and increased electrochemical stability window.

A common feature for highly concentrated electrolytes and ionic liquids is an ordering on mesoscopic length scales, normally not found in simple liquids, resulting from the correlation between the ions. This nanostructure can be expected to influence the ion transport and a key to developing these new electrolyte concepts is to understand the structure and dynamics on mesoscopic length scales and how this links to macroscopic transport. In this thesis, the microscopic properties of ionic liquids and diluted ionic liquids are investigated together with highly concentrated electrolytes based on an organic solvent. To achieve this goal X-ray and neutron scattering are invaluable tools as they allow for measurements at the time and length scale of typical molecular motions and interactions. Complementary techniques such as conductivity and viscosity measurements, differential scanning calorimetry, and Raman spectroscopy have been used in order to link between the macroscopic and microscopic properties and between local structure and dynamics.

Keywords: Ionic Liquid, Electrolytes, Highly concentrated electrolytes, Structure, Dynamics, Ion Transport, QENS, SAXS.

List of Publications

This thesis is based on the work in the following papers:

I *Pressure and Temperature Dependence of Local Structure and Dynamics in an Ionic Liquid*
F. Lundin, H. W. Hansen, B. Frick, D. Rauber, R. Hempelmann, O. Shebanova, K. Niss and A. Matic
Journal of Physical Chemistry B **2021**, *10*, 2719-2728

II *Structure and Dynamics in Highly Concentrated Electrolytes*
F. Lundin, L. Aguilera, H.W. Hansen, B. Frick, S. Lages, A. Labrador, K. Niss and A. Matic
Physical Chemistry Chemical Physics **2021**, *23*, 13819-13826

III *Ion Dynamics and Nanostructure of Diluted Ionic Liquid Electrolytes*
F. Lundin, A. Idström, P. Falus, L. Evenäs, S. Xiong and A. Matic
Submitted for publication, under review

IV *Effect of Water on Local Structure and Dynamics in a Protic Ionic Liquid based electrolyte*
F. Lundin, T. Stettner, P. Falus, A. Balducci and A. Matic
Manuscript

V *Role of Cation on Local Structure and Dynamics in Highly Concentrated Acetonitrile-based Electrolytes*
F. Lundin, J. P. Embs and A. Matic
Manuscript

List of Publications Not Included in the Thesis

I *Density scaling of structure and dynamics of an ionic liquid*
H.W. Hansen, F. Lundin, K. Adrjanowicz, B. Frick, A. Matic, K. Niss
Physical Chemistry Chemical Physics **2020**, *22*, 14169-14176.

II *High-frequency dynamics and test of the shoving model for the glass-forming ionic liquid Pyr14-TFSI*
K. L. Eliasen, H.W. Hansen, F. Lundin, D. Rauber, R. Hempelmann, T. Christensen, T. Hecksher, A. Matic, B. Frick and K. Niss
Physical Review Materials **2021**, *5*, 065606

Contribution Report

I I planned the SAXS experiment that was performed together with co-authors and took part in the QENS experiment. I performed all data analysis and wrote the first draft of the paper.

II I planned the QENS experiment that was performed together with co-authors. I did the data analysis and wrote the dynamics part of the paper, and finalised the manuscript.

III I planned, performed and analysed all experiments apart from the NMR and symmetric cycling. I wrote the manuscript.

IV I planned, performed and analysed the QENS experiment. I did the SAXS experiment and data analysis. I wrote the manuscript.

V I planned, performed and analysed all experiments.
I wrote the manuscript.

Table of Contents

Chapter 1

Introduction

Batteries are becoming an ever increasing part of our lives with applications ranging from internet of things, to electric vehicles and grid storage. Lithium-ion batteries have for a long time been, and still are, dominating on the market for portable devices. Over the years since its commercialisation in 1991 [1] the lithium-ion battery has been under constant development. However, the electrolyte concept has basically been unchanged, being based on the lithium salt $LiPF_6$ dissolved in carbonate solvents. Unfortunately, these electrolytes are highly flammable and the salt decomposes into hazardous gases above 80°C [2], hence a safer electrolyte is preferred. To further develop the lithium ion battery an electrolyte that also allows for higher operating voltages is also desired as it could increase the energy density. To achieve this, new electrolyte concepts are needed to further develop Li-ion batteries and several routes have been pursued, such as, polymer electrolytes [3], inorganic solid electrolytes [4, 5], highly concentrated electrolytes [6, 7] and ionic liquids [8], out of witch the two latter ones have been investigated in this thesis.

After decades of development the lithium ion technology is approaching its maximum theoretical capacity. To take the next step we have to go to new battery chemistries. One of these concepts is the use of a lithium metal anode and the electrolyte is a key component in the realisation of these systems. With current commercial electrolytes plating and stripping of Li during cycling results in the growth of dendrites and a mossy morphology with the formation of dead lithium [9, 10]. In addition, the solid electrolyte interphase (SEI) on Li-metal formed in carbonate based electrolytes is unstable, leading to a continuous consumption of the electrolyte and active Li. It has been found that the use of ionic liquid electrolytes and highly concentrated electrolytes can be a route to solve also these issues [9].

Ionic liquids and highly concentrated electrolytes are both ion-rich liquids. Hence, ionic interactions have a strong influence on their properties and also

leads to ordering in the liquid on the mesoscopic length scale [11, 12]. This ordering, or nanostructure, is typically not found in simple liquids and can be expected to influence the ion transport. Hence, it is of great importance to not only study the ion transport mechanism but also the local structure to fully understand the transport properties of the electrolyte. In organic solvent based electrolytes the amount of salt controls the structure, at low salt concentrations the solvation shells of lithium ions are isolated from each other by free solvent molecules. As the salt concentration is increased less free solvent molecules will be available leading to direct contact of the solvation shells. In ionic liquids, that consists only of ions, the nanostructure manifests as charge ordering, i.e. a repeatable characteristic distance between similar charges. In cases of long alkyl chains on the cation ordering of apolar domains can also be present. Most studies on the structure of highly concentrated electrolytes are based on simulations while the experimental studies still are few. Here we experimentally answer questions such as what happens to the structure when pressure is applied? How is the structure affected when a diluent is introduced to the system? And how is the ionic liquid structure changed when exposed to water?

In the more dilute electrolytes such as commercial electrolytes for lithium batteries, where the solvation shells are well separated a vehicular mechanism controls the ion transport [13]. It means that the whole solvation shell travels as one unit with the active ion through the electrolyte. The ion transport in highly concentrated electrolytes is not expected to be controlled by vehicular mechanisms [14], however, exactly what mechanism it is, is not fully understood. Here we aim to answer questions about the effect of salt concentration on the ion transport in electrolytes, how a diluent influences the dynamics in ionic liquid electrolyte and how the molecular relaxations relates to the conductivity.

In this thesis the local structure of ionic liquids and highly concentrated electrolytes is experimentally investigated using small-angle X-ray scattering (SAXS) and Raman spectroscopy, giving information for instance about the size and composition of the lithium ion solvation shell. The ion transport is investigated on several length and timescales, ranging from macroscopic dynamics like the conductivity, to microscopic dynamics investigated with quasi-elastic neutron scattering (QENS). QENS is an excellent tool to experimentally investigate the dynamics in this type of liquids as it probes the dynamics at relevant scales of time (1 ps-10 ns) and space (1-100 Å) simulta-

neously. Thus, it covers the length scales of the nanostructures found in ionic liquids and highly concentrated electrolytes.

Chapter 2

Electrolytes

In a battery the role of the electrolyte is to efficiently transport ions in between the anode and the cathode. This implies that a high ionic conductivity in the temperature range of the application is needed [15]. It is also essential that the electrolyte is non-conducting for electrons, so that they are forced to go through an external circuit rather than through the electrolyte to reach the opposite electrode. The electrolyte should also be thermally, chemically and electrochemically stable in the desired voltage window, typically 0-5 V [16]. On top of these properties the chemicals used should be non toxic and from a commercially point of view cheap and abundant. Unfortunately, there is so far no electrolyte that fulfils all these requirements and for each application a prioritisation of the properties has to be made to satisfy the most important criteria. There are several kinds of electrolyte concepts such as solid, polymer and liquid electrolytes, all with different advantages and disadvantages. For lithium batteries liquid electrolytes are most common due to a high ionic conductivity (1-10 mS/cm at room temperature) [17]. Additionally for liquid electrolytes it is important that the electrolyte has a low enough viscosity to ensure wetting of the separator and electrodes in the cell and a wide working temperature range and low vapour pressure [16].

A liquid electrolyte consists of a solvent and a salt. The salt is essential for the ion transport and the solvents role is to dissolve the salt. For the choice of solvent the dielectric permittivity and viscosity is of particular importance. A high dielectric permittivity helps dissociation of the salt while a low viscosity will facilitate fast ion transport. Usually two or more solvents need to be combined for the electrolyte to have both properties, as in the case of LP30, a commercially used electrolyte, where 1 M of the salt $LiPF_6$ is dissolved in equal parts of ethylene carbonate (EC) and dimethyl carbonate (DMC). EC has a high dielectric permittivity and creates a passivating layer in the first cycle on the interface between the anode and the electrolyte that prevents further decomposition of the electrolyte during cycling. However, EC has a

high melting point, around 36 °C [18], which makes it unsuitable for room temperature applications. The addition of DMC to the electrolyte lowers the melting point and lowers the viscosity of the solution. To further tailor the properties to better fit the requirements of a particular application additives can be introduced to the electrolyte formulation [19].

Despite being one of the most popular commercial electrolytes on the market, there is still safety concerns associated with using LP30. The organic solvents are flammable and volatile and the salt is chemically unstable [20–22]. This calls for further research towards safe and highly performing electrolytes. Promising alternatives are highly concentrated electrolytes and ionic liquids [10,23], where the lack of free solvents, or in the case of ionic liquids the lack of traditional solvents at all, provides conditions for a safer electrolyte.

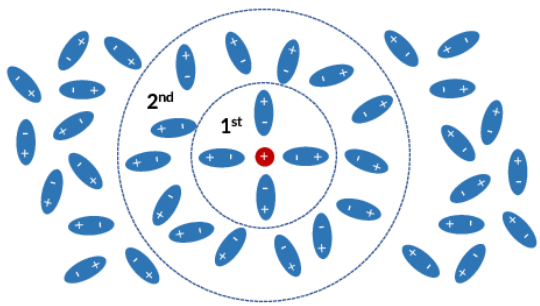

Figure 2.1: Schematic illustration of solvent molecules structured around a cation.

Many of the properties such as conductivity, and stability of an electrolyte are related to the local electrolyte structure [24,25]. The solvation shell in a traditional liquid electrolyte is a result of the solvent molecules arranging themselves around the charged species, due to an electromagnetic dipole-moment in the otherwise neutral solvent molecules enabling interactions between the solvent and ions. Figure 2.1 shows a schematic arrangement of solvent molecules around a cation. The small and symmetric shape of the cation results in a spherically symmetric electrical field, causing the solvent molecules nearby to align. This is referred to as the first solvation shell and is marked in the figure. Outside of the first solvation shell a second solvation shell can also be defined. Even though the strength of the field is heavily reduced as the

distance from the ion increases there can still be some ordering. However, outside the second solvation shell the charge of the cation is screened and there is usually hardly any ordering left. This image of the local structure is only valid for low concentrations where the ions are fully separated and anions are not part of the solvation shell of the cation.

The ionic conductivity, σ, of a material is described the by

$$\sigma = \sum_i n_i q_i \mu_i \tag{2.1}$$

where n_i is the number of charge carriers, q_i their net charge and μ_i their mobility of the ionic species in the electrolyte. For lithium and sodium electrolytes the net charge is fixed to one, hence to increase the conductivity either the number of charge carriers must increase or their mobility. It is important to remember that the conductivity, as indicated by Equation 2.1, sums over all charged species, i.e. not only provides a measure of e.g. lithium transport.

The ion transport in electrolytes at relatively low salt concentrations is well described by a vehicular transport model [13]. In this scenario the ion moves along with its solvation shell through the liquid. It can be approximated as a sphere moving in a viscous liquid and follows the Stokes-Einstein relation of the diffusion coefficient

$$D = \frac{k_b T}{6\pi r_s \eta} \tag{2.2}$$

where k_b is Boltzmann's constant, T is the temperature, r_s is the size of the solvation shell and η is the viscosity. However, this is only valid for very dilute electrolytes where the interactions between ions are negligible [13], for higher concentrations the ion transport is more complex [26–28].

The temperature dependence of the viscosity of liquid electrolytes show a non-Arrhenius behaviour and is well described by the VFT-function

$$\eta = \eta_0 \exp\left(\frac{B}{T - T_0}\right) \tag{2.3}$$

where η_0 is a constant, T_0 is defined as the ideal glass transition temperature and B is a constant related to the fragility of the material [29–31]. The fragility is a measure of how much the temperature dependence of the viscosity deviates from the ideal Arrhenius behaviour. A similar expression to 2.3 can be written

for the ionic conductivity

$$\sigma = \sigma_0 \exp\left(\frac{-B}{T - T_0}\right) \tag{2.4}$$

where the parameters have equivalent meaning as in the viscosity equation.

Chapter 3

Highly Concentrated Electrolytes

The salt concentration of an electrolyte is often chosen to maximise the conductivity and is in general around 1 mol/dm^3. Above this concentration the conductivity decreases as a result of a viscosity increase, therefore higher concentrations have previously not been considered as alternatives [6]. However, this changed when Yamada et al. showed that an electrolyte with a salt concentration of 3.2 mol/dm^3 of the salt LiTFSI in the solvent dimethyl sulfoxide, did not exhibit co-intercalation of the solvent into natural graphite [32]. They attribute this altered property to a change in the solvation shell of the lithium ions. Thus, at high salt concentration a different local structure is envisaged and as a result, the properties of the electrolyte are changed and by that also the transport mechanism can be expected to change. Sou et al. investigated the effect of increased salt concentration in an aqueous electrolyte and found similarly that the properties of the electrolyte changed [33]. Aqueous electrolytes are limited to run below 1.23 V, however, Sou et al. showed that with 21 M LiTFSI in water, the electrochemical stability window increased to 3 V vs Li|Li$^+$. Hence, adding large amounts of salt to the electrolyte enables the use of organic solvents or water that previously have been disregarded due to unfavourable properties at lower salt concentrations. Since the first presented study many highly concentrated systems have been investigated based on solvents such as propylene carbonate [34], acetonitrile [35], ethers [36], glymes [37] and water [33].

These highly concentrated electrolytes (HCEs) can be made safer than LP30 [6, 37–40]. When designing the electrolyte there is a large number of solvents and salts available to choose from. To ensure non-flammability a non-flammable solvent can simply be chosen. However, common non-flammable solvents have been found to have poor passivation ability of the electrode [10]. This on the other hand can be solved by choosing the right salt. It has been shown that

as opposed to the electrolytes with low salt concentration, where breakdown of the solvent is leading to the formation of the protective solid electrolyte interphase (SEI) at the electrode, for highly concentrated electrolytes the SEI is to a large extent formed by anions [10]. The salt can then be selected to create a stable and highly ion conducting SEI and the potential problems of using non-flammable solvents are eliminated. In the highly concentrated electrolytes also the volatility of the solvent is reduced due to the increased interactions between the cations and solvent molecules [10].

Whereas the safety aspect initially might have been the driving force, highly concentrated electrolytes have shown several other advantages compared to conventional electrolytes. Yamada et al. showed with cycling experiments that using a 4.5 M LiFSI/actonitrile electrolyte resulted in a higher capacity during fast charge and discharge of a graphite/lithium metal half cell compared to a cell using LP30 for C-rates up to 5C [35]. It is well known that intercalation kinetics limits the charge rate of lithium ion batteries with graphite electrodes and the fact that a highly concentrated electrolyte outperformed a conventional electrolyte points towards faster intercalation kinetics when using the HCE [35]. Moreover, the use of HCEs can help achieve higher energy density than state-of-the-art batteries by expanding the voltage window of operation of the cell. Wang et al. [40] used a highly concentrated 5.5 M LiFSI/DMC electrolyte to realise stable cycling of a 5V-class electrode as opposed to the 4V-class electrodes that are used with LP30 on the market today.

HCEs have also been investigated as electrolytes for next generation chemistries such as, Li-O_2, Na-O_2 and Li-S batteries. One of the major issues with Li-S cells is the dissolution of polysulfides in the electrolyte during cycling [41]. However, highly concentrated electrolytes have been shown to prevent this dissolution. Since the solubility of a salt has a certain saturation degree for a given solvent and the polysulfides can be considered a salt, the highly concentrated electrolyte will inhibit the dissolution since is already close to saturation before contact with the polysulfides [42, 43]. Another issue for lithium-metal batteries, such as Li-S and Li-O_2, is dendrite formation on the lithium anode and there are reports of highly concentrated electrolytes mitigating this problem. Qian et al. have reported suppression of dendrite growth for over 1000 cycles in a Li-Cu cell in a 4M LiFSI/DME electrolyte [44].

However, there are some shortcomings of highly concentrated electrolytes. The large amount of salt needed increases the cost of the electrolyte consid-

erably. The second issue is that the high viscosity that comes with the high salt concentration causes problems with poor wettability of the separator and electrodes [10]. A suggested solution to the problem is to dilute the highly concentrated electrolyte with another solvent with low viscosity. This is further discussed in section 3.3.

3.1 Structure

The development of HCE has to a large extent been empirically driven and in many respects a fundamental understanding of the local structures and dynamics is lacking. The change in physical and electrochemical properties has been suggested to be an effect of changes in the local structure [6]. Figure 3.1 shows a schematic of how the local structure changes with salt concentration. For low salt concentrations there are plenty of free solvent molecules and the first solvation shell of the cations consists of solvent molecules. As the salt concentration increases more molecules will be needed to solvate the cation until a point where there will be almost no free solvent molecules left in the electrolyte. With the salt concentration increasing the number of anions in the electrolyte increase to a point where they will not be fully separated from the cations but also start taking part in the first solvation shell.

There are a few experimental studies of the development of the local structure as the salt concentration increases performed with Raman spectroscopy. These studies show that with increasing salt concentration the number of free solvent molecules are reduced to a limit where all solvent molecules are coordinated to a cation ion [35, 36, 40, 45]. For the higher salt concentrations also the anion takes part in the solvation shells with contact ion pairs and aggregates being formed. Yamada et al. report that for 3.2 M of LiTFSI in DMSO, all TFSI anions and DMSO molecules are coordinated to lithium ions and form a polymetric fluid network of Li^+ and TFSI [45]. SAXS provides a global view of the solution structures, such as clusters, aggregates and nanodomains. Aguilera et al. [46] used SAXS to investigate the structure in LiTFSI-tetraglyme (G4) mixtures from dilute to highly concentrated solutions. In the neat solvent G4 only one peak at Q=1.5 $Å^{-1}$ appears, corresponding to the nearest neighbour distance. With increasing salt concentration a second peak around Q=0.95 $Å^{-1}$, which corresponds to a 6.6 Å distance in real space appears. This distance is attributed to alternating charges, similar to that found in ionic liquids. A

similar study was performed on a siloxane based electrolyte with 5 M of LiTFSI by Amine et al. [47], where a second peak appeared in the Q-range from 0.5-0.8 $\mathring{A}^{-1}$. They attribute this peak to the formation of aggregates.

Paper II and V in this thesis investigate the structure in acetonitrile based electrolytes using LiTFSI and NaTFSI as a function of salt concentration. The different number of coordinating solvent molecules for the Li^+ and Na^+ predicts the solvation shells to differ in size while maintaining similar structure.

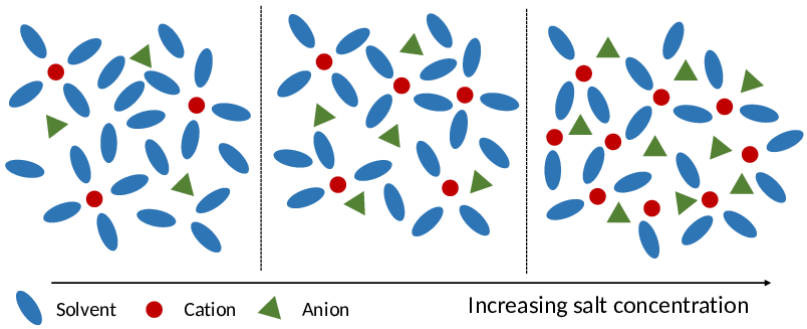

Figure 3.1: Schematic of local electrolyte structure as a function of salt concentration.

3.2 Ion transport

The ion transport mechanism of HCEs differs from conventional electrolytes where vehicular ion transport is dominating. With no free solvent molecules in the electrolyte the cations cannot travel with their solvation shell. One proposed model of ion transport in HCEs is ligand exchange where the association and dissociation between the cation and the solvent molecules, or anions, is the fundamental process [27] rather than having the entire solvation shell moving as in vehicular transport [13]. Another model, that is described for highly concentrated aqueous electrolytes, is that the electrolyte undergoes phase separation into nanosized anion-rich domains, where the anions are rather immobile, and H_2O rich domains with cations dispersed [28]. Fast ion transport is then still possible through a vehicular mechanism in a network of H_2O. Based on results published the ion transport seems to be heavily dependent on the actual system.

Seo et al. published a study in 2013 where they, through molecular dynamics simulations, investigated the dynamics in acetonitrile based electrolytes with varying salts and salt concentrations [48]. They found that the anions stayed coordinated to lithium ions for a longer time than they were interacting with the solvent molecules. The anion-Li^+ residence time was found to vary with the different types of anions and for the TFSI-anion the residence time increased with the salt concentration, from ∼350 ps for 30AN:1LiTFSI up to ∼700 ps for 5AN:1LiTFSI. However, this trend was not seen for all salts. For the BF_4 anion a reversed behaviour was observed with shorter residence time for higher concentrations. Considerably shorter residence times were presented by Okoshi et al. for NaTFSI in DME and concentrations up to 40 mol% [27]. From molecular dynamics they found a life time of the solvation shell to be around 120 ps. A recent study by Åvall et al. present even shorter residence times [49]. By investigating the ligand exchange rates in PC and acetonitrile electrolytes with concentrations of $LiPF_6$ and $NaPF_6$ from 20:1 to 5:1 using ab initio molecular dynamics have found residence times of 1-15 ps. A decrease in residence time was seen with concentration for both electrolytes in agreement with the trend for the BF_4 anion [48]. They also found that the Na-salt electrolytes show a shorter residence time than the lithium equivalents [49].

Most studies reported so far are based on simulations and the interaction behaviour and residence times differ largely in studies for various solvents/salts. It is at present not clear if the large difference comes from actual differences in the system or from different simulation techniques and definitions of when a molecule is in the solvation shell. Therefore, as always, it is important to verify the results with experiments.

One of few experimental studies of local dynamics in highly concentrated electrolytes was performed by Dokko et al [50]. From NMR measurements an unusually high lithium self-diffusion in a sulfolane based electrolyte was observed. This study showed that lithium diffused faster than both the anion and the solvent molecules. This is not in line with the vehicular model, where the lithium is transported in a solvated form together with either anion and/or solvent molecules. They attributed this increased lithium diffusion to an additional jump diffusion [50], resulting in a mix of vehicular transport and jump diffusion. When looking at local dynamics experimentally another suitable tool is neutron scattering. With quasi-elastic neutron scattering one can access both the time and length scale of the motions of the ion transport

and directly compare it to MD simulations. However, there are only few studies on highly concentrated liquid electrolytes using QENS. In paper II and V the ion transport in highly concentrated acetonitrile based electrolytes is investigated using QENS. Furthermore, by using two different salts, LiTFSI and NaTFSI, the effect of the cation is studied in these highly concentrated electrolytes.

3.3 Diluted Highly Concentrated Electrolytes

Highly concentrated electrolytes have high viscosity which can cause poor wetability of the separator and electrodes. Moreover, the conductivity can be a bit too low and in order to address that and the high viscosity the electrolyte can be diluted. Diluting a highly concentrated electrolyte might sound contradicting, but it depends on how it is done. A successful dilution should lower the viscosity while maintaining the favourable properties induced by the high salt concentration. To do that the diluent must fully mix with the electrolyte while not interacting with the Li-ions (or other salt cation) to preserve their solvation structure. Additionally it should also be stable towards other cell components [12]. Diluting the electrolyte also lowers the amount of salt needed and hence reduces the cost (provided that the price of the diluent is low).

One class of solvents that has been found to work well as diluent for highly concentrated electrolytes is hydrofluoroethers (HFEs). The key to the success of dilution using HFEs is their unique poor lithium solvating behaviour [51], that originates from the electronegativity of the fluorine. The Li^+ normally coordinates with the oxygen of the ether molecule, however, with the fluorine atoms pulling the lone electron pairs of the oxygen the oxygen can be left electropositive. The number of fluorine on the molecule is of importance for the lithium solvating ability of HFE, yet it is critical to also consider the location of the fluorine atoms in the molecule [51]. Figure 3.2 show some HFEs commonly used for dilution, where bis(2,2,2-trifluoroethyl) ether (left) with no fluorine at carbons closes to the oxygen has higher lithium solvating ability than the 1,1,2,2-tetrafluoroethyl- 2,2,2-trifluoroethyl ether (middle) and 1,1,2,2-tetrafluoroethyl-2,2,3,3-tetrafluoropropyl ether (right) where the fluorine atoms are located closer to the oxygen.

HFEs have successfully been used as diluents for several electrolyte concepts, including highly concentrated DME based electrolytes [52, 53], glyme based

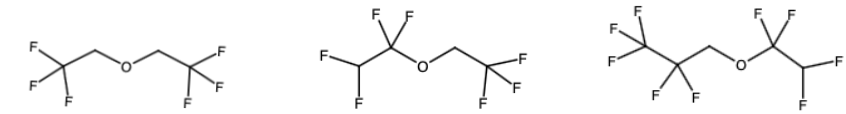

Figure 3.2: Structures of some HFEs commonly used for dilution of highly concentrated electrolytes.

solvate ionic liquid electrolytes [43, 54] and ionic liquid electrolytes [55–58]. While in all of these studies the viscosity was lowered while maintaining the solvation structure intact, there are other benefits of adding HFE to the electrolyte. The SEI formed on lithium metal anodes were found to be more stable with fluorinated diluents in the electrolyte [53] and it has also been found to decrease the dissolution of poly-sulfides into the electrolyte in Li-S cells [54].

Adding too much diluent will eventually affect the solvation structure, Beltran et al. investigate the structure of LiFSI in dimethyl carbonate (DMC) with varying concentration of HFE [59]. They find that at low diluent concentrations, the network of highly concentrated electrolyte is connected in a three dimensional solution structure. However, when the diluent concentration is higher than the molar ratio 0.58LiFSI:1DMC:1.5HFE (corresponding to 1.77 M), the three-dimensional solution structure is separated by the diluent into island-like solvation complexes. This "over dilution" was also found by Lu et al. when a glyme based electrolyte Li(G4)TFSI was diluted with too much HFE (1Li(G4)TFSI:4HFE) the cycle capability of a Li-S cell started to decrease [54].

While the result from previous studies show promising results they have to a large extent focused on macroscopic properties of the diluted highly concentrated electrolytes, such as conductivity and cycling performance. There is still a lack of microscopic understanding of the effect of dilution on the structure and ion transport mechanism in these systems. In paper III closer attention is paid to the structure and dynamics of a diluted ionic liquid electrolytes using techniques such as Raman spectroscopy, SAXS, NMR and QENS.

Chapter 4

Ionic Liquids

Ionic liquids are salts that are liquid at relatively low temperatures [60]. The definition varies slightly, but a common one in literature is that ionic liquids are salts with a melting point below 100 °C [61]. The low melting point of ionic liquids comes from the large size of the anions and cations and a charge delocalisation that together with asymmetry of the ions prevents efficient packing and therefore also crystallisation. There is a large number of anions and cations suitable for ionic liquids and when designing an ionic liquid for a specific area of application there are many combinations to choose from in order to tailor the properties of the liquid [62]. Ionic liquids can be divided into subgroups of aprotic and protic ionic liquids, where protic ionic liquids have an available proton on the cation that enables hydrogen bonding [63]. The two subgroups have similar properties but protic ionic liquids have been investigated more for fuel cells while aprotic ionic liquids have been considered for electrolytes for supercapacitors and batteries [64]. Figure 4.1 shows a few of the cations and anions that are commonly used for battery applications [64].

Ionic liquids are good alternatives to organic solvents in electrolytes. First of all they are thermally stable and nonflammable which increases the safety aspect of the electrolyte [19]. On top of that they have a fairly high ionic conductivity, a large electrochemical stability window and are good solvents for many Li-salts [19]. Even though ionic liquids are salts, an addition of a lithium-salt is needed to make a Li battery electrolyte. Adding salt to the ionic liquid increases the viscosity [65], decrease the conductivity [66], and increases the glass temperature (T_g) [66].

In the initial cycles the anions have been found to break down to form the SEI [67], hence, the choice of anion in the ionic liquid can affect the stability of the SEI. Unfortunately, there are also drawbacks to the ionic liquid in battery applications, just like in the case of highly concentrated electrolytes, ionic liquids suffer from high viscosity as well as high cost [19]. A way to reduce

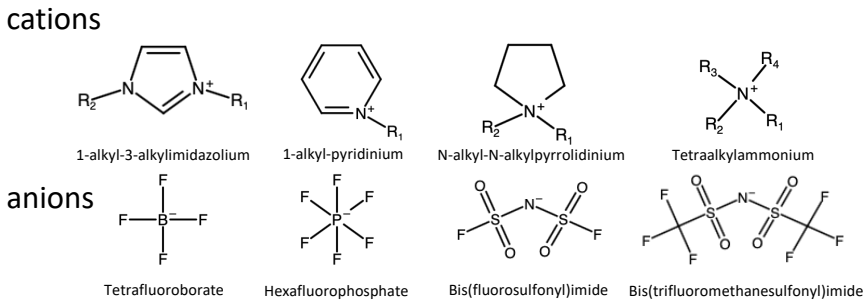

Figure 4.1: Structures of some common cations and anions in ionic liquids.

both the cost and the viscosity of ionic liquids is to mix them with low viscosity solvents [19]. Dilution can in the best case preserve the good properties of the ionic liquid while mitigating the drawbacks. Earlier in the thesis diluted ionic liquid electrolytes were discussed in section 3.3 and the dilution of neat ionic liquid with water will be further covered in Section 4.3.

4.1 Structure

As in the case of the highly concentrated electrolytes, the favourable properties of ionic liquids come from the local structure. The absence of neutral molecules leaves us with only charged species that give rise to charge ordering. This has been confirmed amongst others, Mackoy et al. in a MD simulation where the structure factor of 1-butyl-1-methylpyrrolidinium bis(trifluoromethylsulfonyl)imide (P14TFSI) showed two peaks [68]. The first peak, which is also found in simple liquids, represents the distance between molecules, a nearest neighbour distance of 4-5 Å. The second peak was, with the help of partial structure factors, assigned to originate from the reoccurring distances between two anions or two cations of 7-8 Å, hence there is a charge ordering with alternating charges found in ionic liquids that is typically not found in simple liquids. The distance between the similar charges is expected to vary with the size of the ions, e.g an ionic liquid with a TFSI anion is expected to show a larger separation between similar charges than an ionic liquid with a BF_4 anion. A third peak can be seen around 0.35 $Å^{-1}$ in ionic liquids with alkyl chains of 6 carbons or more [69]. Triolo et al. was first to

provide experimental evidence of the existence of this nanoscale segregation in ionic liquids, using X-ray diffraction [70]. By systematically vary the length of the cation side chains the origin of the peak was confirmed. The origin stems from the formation of apolar domains in the ionic liquid. These heterogeneities are around 20 Å and originate from the segregation of the alkyl chains due to van der Waals interactions. Understanding the structure and dynamics on the local scale is thus of importance to understanding the ion transport in a potential electrolyte use.

The influence of Li-salt (LiTFSI) on the structure of ionic liquids based on pyrrolidinium (Pyr) and imidazolium (Im) cations and the TFSI anion was studied with SAXS by Aguilera et al. [69]. They found that the peak related to formation of apolar domains was barely affected by the addition of lithium salt. However the charge ordering peak decreases in intensity and shifts to slightly lower Q-values, indicating a longer distance between similar charges. This is believed to stem from the formation of $Li[TFSI]_2$ triplets [71, 72].

4.2 Dynamics

The conductivity and viscosity in ionic liquids and ionic liquid electrolytes does not follow the Arrhenius behaviour, but is well described with a VFT-function, as for all liquids [66, 73–76]. Scaling of the conductivity with T_g have showed that ionic liquids with varying salt concentration fall on the same master curve, implying that the ionic conductivity have the same temperature dependence for all salt concentrations [77].

It is the microscopic motions in the ionic liquid that sums up to the macroscopic properties like conductivity. While the conductivity is easily studied it takes more complicated methods to investigate the local dynamics. For example NMR was used by Marzan and Boltoeva to investigate the self-diffusion of an imidazolium based ionic liquid [78]. By varying the alkyl chain length n of the imidazolium cation, $C_n$mim, they found that the longer the chain the slower self-diffusion. It was also found that the cation had a higher mobility than the TFSI-anion for chain lengths below 6, while above that, the two ions had similar diffusion coefficients [78]. While changing the length of the alkyl chain the balance between coulombic forces and van der Waals interactions is modified which gives rise to changes in the dynamics. Hence, the composition

of the ionic liquids plays a role in the diffusional behaviour.

NMR studies of P14TFSI and P14FSI with added LiTFSI and LiFSI respectively, show that the relative mobilities between the ions differ [79]. In the P14TFSI:LiTFSI electrolyte the P14 cation show the highest mobility whereas in P14FSI:LiFSI the FSI anion is faster. Surprisingly the diffusion of the Li^+ is slower than the larger bulkier P14 cation in both electrolytes. This is an indication that the lithium is interacting with the anions [79]. In fact the lithium is known to form aggregates with the anions, in the shape of triplets e.g. $Li[TFSI]_2$ [71, 72].

To look further into the processes that builds up to the diffusion measured with NMR one can use QENS. Dynamics in pure ionic liquids have been investigated rather thoroughly with QENS [80–84], finding both local relaxations of sections of molecules and diffusional processes of the entire molecules. Kofu et al. investigated the dynamics of imidazolium-based ionic liquids, with varying alkyl chain lengths and different anions as a function of temperature [81]. In this study they find three independent relaxations on time scales of 1 ps to 10 ns. They claim these motions are, presented in order of falling relaxation time, ionic diffusion, in the shape of a jump diffusion, a relaxation of the imidazolium ring and an alkyl chain reorientation. These three motions are self-diffusive motions depending only on the ion itself. In another publication by the same authors [80], a motion of collective dynamics attributed to the heterogeneity in the structure is proposed. This motion is slower than all the self-diffusion processes.

What is still lacking is a link between the macroscopic properties of the ionic liquid such as the conductivity and the local dynamics and structure of ionic liquids. This is addressed in paper I where a combination of dielectric spectroscopy and QENS is used to do this.

4.3 Water in Ionic Liquids

For some applications adding water to an ionic liquid is beneficial to for example lower the viscosity and increase conductivity, for other applications water is detrimental but it is still important to understand what happens *if* water is taken up in the ionic liquid. Therefore investigations of the impact of water in ionic liquids have been done in several fields such as ionic liquids for fuel cell [85] and supercapacitor applications [86] as well as for the fundamental understanding of how it effects the structure and diffusion mechanism [87–89].

The way the water interacts with the ionic liquid varies strongly between different ionic liquids. The hydrophobicity of the anion, the length of the alkyl chains of the cation and whether the ionic liquid is protic or aprotic has all been found to affect the solubility of water [85, 90]. Hence, there are ways to design the ionic liquid to take up more water or less water depending on the intended application. Huddleston et al. investigated the hydrophobicity of imidazolium based ionic liquids with different anions and found that it increases in the order $Cl<I<BF_4<PF_6<TFSI$ [90]. The typical battery anion TFSI is then rather hydrophobic. Longer side chains on the cation are also found to decrease the solubility of water [90]. Protic ionic liquids, with an available proton on the cation, can hydrogen bond to the water molecules, which allows the cation to theoretically directly interact with the water molecules. Hence, protic ionic liquids are in general more prone to take up water than aprotic ionic liquids.

Studies of the structural behaviour of water in ionic liquids have shown that domains form over a certain concentration. However, the limit depends on the specific ionic liquid. In the aprotic ionic liquid, C_4mimBF_4, well defined water clusters was found from SANS measurements when the water weight fraction was greater than 20 wt % [91]. This was further supported by Ruiz-Martín et al. Using QENS they identified both bound water and bulk-like water in the same system [89]. With the BF_4 anion being hydrophilic the water molecules tend to form hydrogen bonds with the anion rather than the cation. An ionic liquid that shows a different behaviour is $P_{H4}TFSI$, a pyrrolidinium based protic ionic liquid. $P_{H4}TFSI$ has a rather hydrophobic anion (TFSI), as compared to the BF_4 anion, and a cation that has the ability to hydrogen bond to water molecules. At low water concentration it is suggested by molecular dynamics simulations that this results in hydrogen bonding by water molecules to both the cation and the anion, where the water becomes a shared solvent molecule [92]. Close to the solubility limit of this ionic liquid, 3.8 wt %, the formation of domains are predicted with a size of six water molecules or more. In these domains some water molecules have only other water molecules in their proximity.

In paper IV $P_{H4}TFSI$ is investigated as a function of water concentration with IR spectroscopy, SAXS and QENS to experimentally investigate how the structure and dynamics change with the addition of water as a complement to the computational study.

Chapter 5

Methods

5.1 Physical characterisation

5.1.1 Density

There are several reasons to measure the density of an electrolyte for battery applications, one is to simply know the weight of the electrolyte in a battery cell. It is also needed to calculate the molar conductivity. In this thesis it has further been used to determine the optimal sample thickness for quasi-elastic neutron scattering.

The density is easily determined as the mass divided by the volume, however, for an accurate measurement of the density a density meter can be used. In this thesis a DMA 4500 M density meter from Anton Paar is used, which allows for an accuracy of up to 5 digits in cm^3/g. The sample is here placed in a U-shaped tube with a known, fixed volume and the whole tube is set into motion by an piezoelectric actuator. The tube will then resonate at different eigenfrequiencies depending on the mass of the sample. Figure 5.1 show an example of the temperature dependence of the density of an ionic liquid electrolyte for different concentration of the diluent HFE.

5.1.2 Viscosity

The viscosity is a measure of a liquids resistance to deformation, or flow. Low viscosity is of high importance in electrolytes, as that directly translates into faster ion transport. Depending on the sample, different techniques to measure the viscosity are suitable. In this thesis a rolling ball viscometer has been used. It is an appropriate technique for samples with a viscosity between 0.1 to 10 000 mPas, which includes ionic liquids and highly concentrated electrolytes. A capillary with known volume is filled with the sample of interest and a metal bead. The viscosity is then calculated from the time it takes for

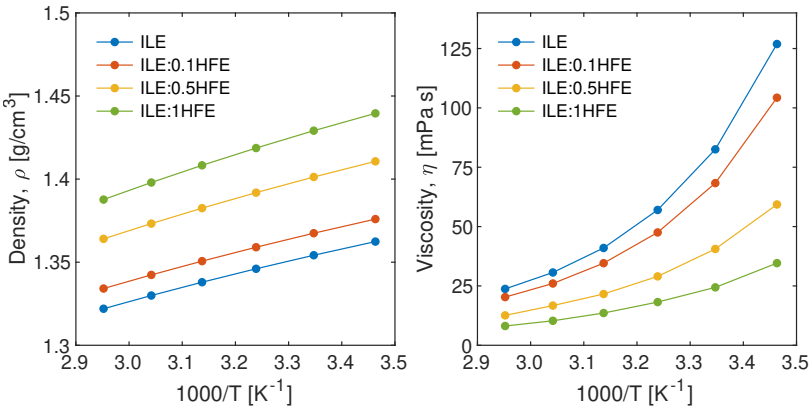

Figure 5.1: Arrhenius plot of the density (left) and the viscosity (right) of an ionic liquid electrolyte, P14FSI:0.2LiFSI, with varying dilution of hydrofluoroether.

the metal bead to fall through the liquid. Figure 5.1 shows an example of the temperature dependence of the viscosity of an ionic liquid electrolyte for different concentration of the diluent HFE.

5.1.3 Conductivity

In this thesis the ionic conductivity has been measured with dielectric spectroscopy via the dielectric permittivity, ϵ^*. In the experiment an alternating voltage is applied to the sample, a schematic of the sample cell is seen in Figure 5.2, and the resulting alternating current is measured. The impedance is then calculated using Ohms law. Equation 5.1 shows the relation between the current J, the voltage E, the Impedance Z and the dielectric permittivity,

$$\epsilon^*(\omega) = \frac{J^*(\omega)}{i\omega\epsilon_0 E^*(\omega)} = \frac{1}{i\omega Z^*(\omega) C_0} \tag{5.1}$$

where C_0 is the vacuum capacitance of the system [93], which is given by

$$C_0 = \epsilon_0 \frac{A}{d} \tag{5.2}$$

where A is the area of the electrodes in between which the material is placed and d is the distance between the electrodes.

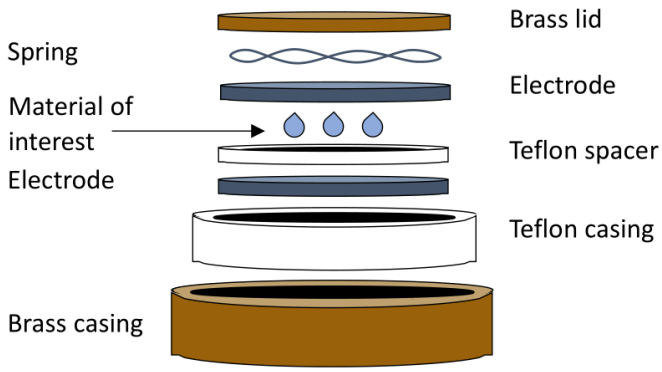

Figure 5.2: Sample cell for dielectric spectroscopy measurements.

The real part of the conductivity σ' of a material is related to the imaginary part of the permittivity [94]

$$\epsilon^*(\omega) = \epsilon'(\omega) + i\epsilon''(\omega) = \epsilon'(\omega) + i\frac{\sigma'(\omega)}{\omega}. \tag{5.3}$$

The DC-conductivity is the part of interest when investigating the conductivity of an electrolyte. It is found as the plateau in the curve of $\sigma'(\omega)$ seen in Figure 5.3 [93].

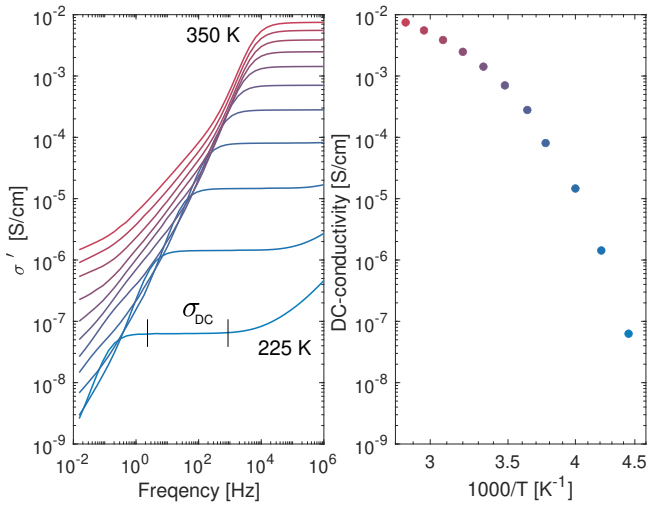

Figure 5.3: Left: Frequency dependent conductivity of a highly concentrated acetonitrile-based electrolyte, LiTFSI:2ACN, in the temperature range 225-350 K. The DC-conductivity is found as the plateau in the frequency dependence of the real part of the conductivity as indicated in the figure. Right: Temperature dependence of the DC conductivity of LiTFSI:2ACN.

5.1.4 Differential Scanning Calorimetry

Differential scanning Calorimetry (DSC) is a tool to investigate thermal transitions in a material. In a battery perspective it can for example give you information about the liquid range of the electrolyte. In a DSC measurement the heat flow in or out of a sample is measured as a function of temperature. Thermal transitions are detected as a change in heat flow corresponding to the amount of energy needed to change the temperature of the sample. Figure 5.4 shows an example of a DSC trace for an ionic liquid, where the crystallisation, which is a exothermic process, manifests as a peak, the endothermic melting as a dip and the glass transition as a step in the heat flow curve. When reporting values for the different transitions it is important to clearly define which temperature is reported as several degrees can separate the onset and the mid-point of the transition for example. In this thesis the glass transition temperature is defined as the mid-point.

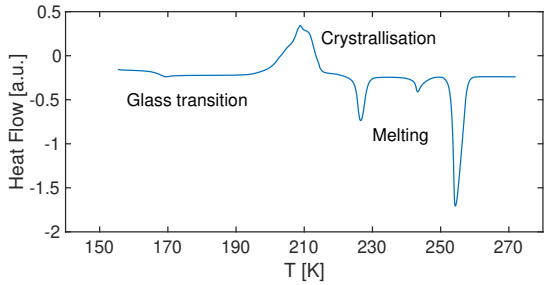

Figure 5.4: DSC trace of an ionic liquid showing a glass transition, crystallisation and melting.

5.2 Small-Angle X-ray Scattering

Small-angle X-ray scattering is sensitive to changes in nano-scale electron density in a material and can therefore be used to probe, for example, size distributions of nanoparticles, pore sizes or characteristic distances in partially ordered materials [95]. Figure 5.5 shows a schematic of a SAXS experiment. An incoming monochromatic X-ray beam with wavevector $\boldsymbol{k}_i$ is scattered off the sample in an angle of 2θ and the scattered intensity is registered by a detector. Equations 5.4 and 5.5 describe the wavevector $\boldsymbol{k}$ and the momentum transfer vector $\boldsymbol{Q}$.

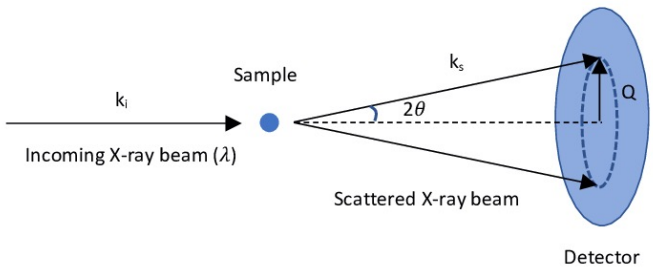

Figure 5.5: Schematic of a small-angle X-ray scattering experiment.

$$|\boldsymbol{k}| = k = \frac{2\pi}{\lambda} \tag{5.4}$$

$$\boldsymbol{Q} = \boldsymbol{k}_s - \boldsymbol{k}_i \tag{5.5}$$

It is convenient to express the scattering pattern in terms of momentum transfer (Q) rather than 2θ since Q includes the information of λ enabling direct comparison of SAXS patterns from experiments when different wavelengths are used. $\boldsymbol{Q}$ can be related to the real space distance through [96],

$$|\boldsymbol{Q}| \sim \frac{2\pi}{d} \tag{5.6}$$

and gives an idea of what length scale the features in the pattern originate from. For elastic scattering events the incoming and scattered wavevector have the same magnitude, $|\boldsymbol{k}_i| = |\boldsymbol{k}_s|$ and Q can be expressed in terms of the scattering angle (θ) as

$$|\boldsymbol{Q}| = Q = 4\pi \frac{\sin\theta}{\lambda}. \tag{5.7}$$

Figure 5.6a shows an example of a two dimensional SAXS pattern of an ionic liquid. The colorbar indicates the intensity of the signal i.e. the normalised number of photons registered by that part of the detector. For isotropic materials, such as liquids, the sample scatters equally in all azimuthal angles (marked as α in the figure) and the 2D pattern can be shown as a 1D pattern, I(Q), by integrating over all the azimuthal angles [97]. An example of such a curve is shown in Figure 5.6b. In this SAXS pattern of an ionic liquid, we see two peaks, related to the presence of characteristic distances in the material. From this type of data, we can determine if there is any type of order in the material, and on what length scales this order appears.

5.2.1 Experimental Considerations

I22 is a small-angle scattering beamline at Diamond Light Source, Oxfordshire, United Kingdom and was used to investigate the structure of ionic liquids in this thesis. There are many elements to take into account when setting up the instrument to suit a certain experiment, the geometry of the instrument, e.g. the incoming energy of the beam and the thickness of the sample. Assuming that the instrument geometry is fixed, i.e. that the sample and detector positions are locked, the angle 2θ that can be covered by the detectors is fixed.

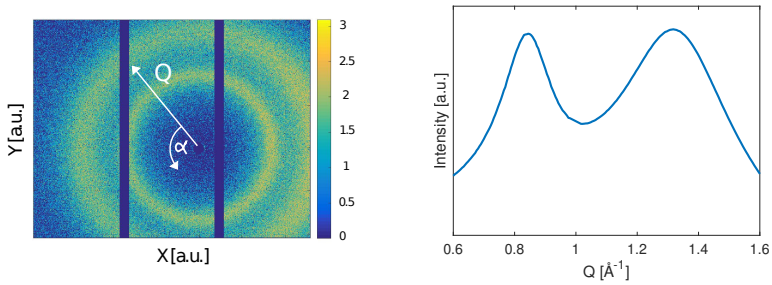

(a) (b)

Figure 5.6: Experimental SAXS data of the ionic liquid P14TFSI in (a) two dimensions and (b) one dimension measured at CMAL, Chalmers University of Technology, Sweden.

Looking back at Equation 5.7, the only parameter left that affects the Q-range is the wavelength/energy of the incoming beam. The incoming energy of the beam at I22 can be varied from 6 to 20 keV and can therefore be selected to fit the Q-range of interest of the sample studied.

What should also be taken into account is the sample thickness. The scattering intensity of a material increases linearly with the thickness, while the absorption increases exponentially. The resulting intensity is then given by

$$I \propto de^{-\mu d} \tag{5.8}$$

where d is the thickness of the sample and μ is the linear absorption coefficient [98]. The intensity function has a maximum transmission for d $=1/\mu$, thus the thickness should be chosen to match the linear absorption coefficient which is material specific and also energy dependent [96].

In order to separate the scattering from the sample from the contribution of the sample cell and the background, a measurement of the empty cell is needed and is later subtracted from the signal. Before subtracting the empty cell and the background the scattered intensity is normalised. In front of the sample a monitor measures the incoming intensity and after the sample a monitor registers the transmitted beam. Using these two intensities a normalisation can be done.

5.3 Raman Spectroscopy

Raman spectroscopy is a technique based on the inelastic scattering of photons where the energy shift gives information about the vibrational modes of the material. It is a useful tool to investigate e.g. the coordination and interaction between species in an electrolyte.

A monochromatic light (photon energy E_i), typically from a laser, impinges on the sample. In a Raman experiment the photon energy is not enough for the molecule to go to an exited electronic state but it ends up in a virtual energy state. From this state the molecule relaxes within a few picoseconds and emits a photon with energy $E_f = E_i \pm \Delta E$ with ΔE being the energy difference from the initial to the final vibrational state of the molecule [99]. There are three cases for the energy shift as seen in Figure 5.7. The first one

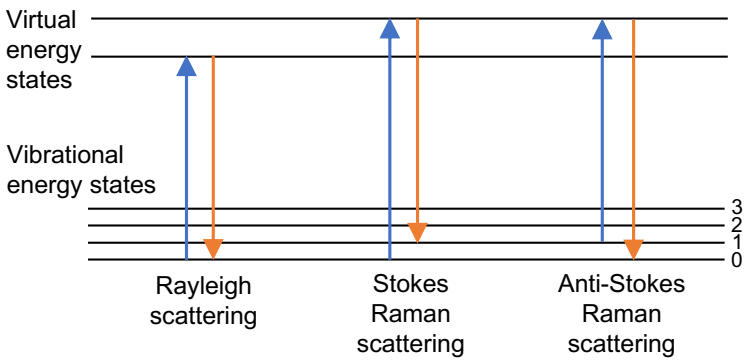

Figure 5.7: Schematic of the Raman scattering process

is elastic scattering, Rayleigh scattering, with $\Delta E = 0$. The excitation and de-excitation are then from the same vibrational energy state. For the two inelastic cases there are Stokes and anti-Stokes. For Stokes the de-excitation happens to a higher vibrational energy state than the origin, resulting in a loss in energy, $\Delta E = -h\nu$. Anti-Stokes start at an exited vibrational state and relax to the ground state, causing a gain in energy, $\Delta E = h\nu$ [99]. In equilibrium it is most common for the molecule to be in its vibrational ground state, and hence the Stokes scattering is typically stronger than the anti-Stokes scattering. The Raman shift is traditionally visualised in wavenumbers, $\tilde{\nu}$,

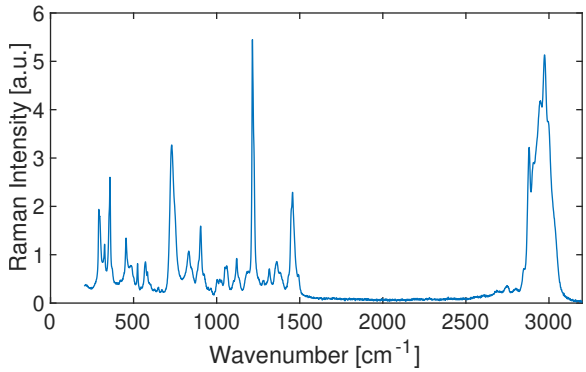

Figure 5.8: Example of Raman spectra of an HFE diluted ionic liquid electrolyte, P14FSI:0.2LiFSI:0.5HFE.

according to

$$\tilde{\nu} = \frac{\nu}{c}$$

and in the unit [cm^{-1}]. An example of a Raman spectrum is seen in Figure 5.8.

5.3.1 Data Analysis

In this thesis Raman spectroscopy is used to investigate the coordination in electrolytes. The vibrational mode measured by Raman spectroscopy is different for free and coordinated molecules. Hence, the energy shift is expected to be different when the molecule is interacting with another molecule. By analysing the band position information about the local surrounding can be obtained. The intensity of the band is also related to the number of molecules with the corresponding vibrational mode which can be used to determine the relative number of certain species. Deconvolution of the spectra can be done to separate contributions from different vibrational modes. An example of a deconvoluted Raman band related to the TFSI anion in a acetonitrile based electrolyte with LiTFSI:5ACN is found in Figure 5.9. The band shape in liquids is well described by the Voigt profile which is a convolution of the Lorentzian and the Gaussian shape and has therefore been used in this thesis. Two clear contributions are found in Figure 5.9, where the low frequency band, Band 1 with area A_1, is attributed to free TFSI ions while the right band, Band 2 with area A_2, is TFSI ions coordinated to lithium ions. The areas of

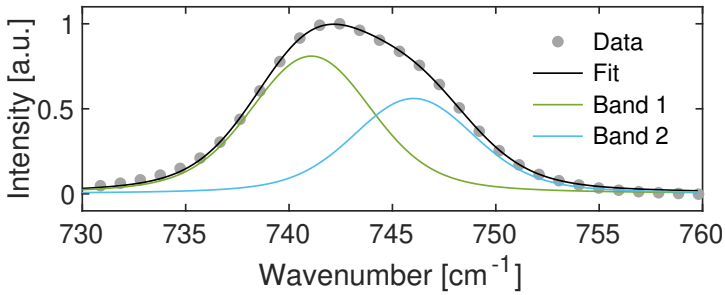

Figure 5.9: Deconvolution of Raman spectra of an highly concentrated acetonitrile electrolyte with LiTFSI, LiTFSI:5ACN.

the two components can be used to determine the fraction of Li^+ coordinated TFSI ions, C_{coord},

$$C_{\text{coord}} = \frac{A_2}{A_1 + A_2} \tag{5.9}$$

which in turn can be used to calculate the average number of TFSI interacting with each Li^+

$$N_{\text{TFSI/Li}} = \frac{C_{\text{coord}}}{x} \tag{5.10}$$

where x is the molar fraction of Li^+ with respect to TFSI [56].

5.4 Quasi-Elastic Neutron Scattering

QENS is a tool to investigate dynamical processes on the typical time and length scales of atomic and molecular dynamics, making it suitable for investigations of for example proteins, polymers and ionic liquids [100]. In a neutron scattering experiment the neutron interacts with the nucleus of an atom. The strength of the interaction is determined by the scattering length, b, which depends on the particular nucleus (isotope) and its spin state. There is no theory to describe nuclear forces well enough to calculate the scattering lengths of nuclei, thus they are experimentally determined. The scattering length varies erratically over the periodic table and also between isotopes [101], some examples are found in table 5.1.

Quasi-elastic neutron scattering is an inelastic method where the energy exchange between the nucleus and the neutron is the sought after quantity. For

Table 5.1: Neutron cross sections

Element	σ_{coh} [barn]	σ_{inc} [barn]	σ_{tot} [barn]
H	1.7568	80.26	82.02
D	5.592	2.05	7.64
Li	0.454	0.92	1.37
Al	1.495	0.0082	1.503

elastic interactions Equation 5.7 was used to express the momentum transfer, Q, in the scattering process. For inelastic scattering $|\boldsymbol{k_i}| \neq |\boldsymbol{k_s}|$ and Q depends not only on the scattering angle but also on the energy change and is given by

$$Q = \sqrt{k_i^2 + k_s^2 - 2k_i k_s \cos(2\theta)}. \tag{5.11}$$

In a quasi-elastic neutron scattering experiment the number of scattered neutrons per second in a solid angle $d\Omega$ with a final energy between E' and E'+dE' are measured and is described by the double differential scattering cross section

$$\frac{d^2\sigma}{d\Omega dE} = \frac{k_s}{k_i}\frac{1}{2\pi\hbar}\sum_{jj'}\overline{b_{j'}b_j}\int_{-\infty}^{\infty}\langle\exp\left(-i\boldsymbol{Q}\cdot\boldsymbol{R}_{j'}(0)\right)\exp(i\boldsymbol{Q}\cdot\boldsymbol{R}_j(t))\rangle\exp(-i\omega t)dt, \tag{5.12}$$

where the index j and j′ run over all nuclei, $\boldsymbol{R}_j$ and $\boldsymbol{R}_{j'}$ are the position of nuclei j and j′ at the time t, $\langle\rangle$ denotes the thermal average and b is the scattering length of the nucleus [101]. This expression describes the inter-particle correlations and their time evolution in terms of position operators of the particles of the scatterer. Under the assumption there is no correlation between the scattering length values, b, of different nuclei

$$\begin{aligned} \overline{b_{j'}b_j} &= (\overline{b})^2, \qquad j' \neq j, \\ \overline{b_{j'}b_j} &= \overline{b^2}, \qquad j' = j. \end{aligned} \tag{5.13}$$

Equation 5.12 can then be expressed as

$$\frac{d^2\sigma}{d\Omega dE} = \frac{k_s}{k_i}\frac{1}{2\pi\hbar}(\overline{b})^2 \sum_{jj'} \int_{-\infty}^{\infty} \langle \exp\left(-i\boldsymbol{Q}\cdot\boldsymbol{R}_{j'}(0)\right) \exp(i\boldsymbol{Q}\cdot\boldsymbol{R}_j(t))\rangle \exp(-i\omega t)dt$$
$$+\frac{k_s}{k_i}\frac{1}{2\pi\hbar}(\overline{b^2} - (\overline{b})^2) \sum_{j} \int_{-\infty}^{\infty} \langle \exp\left(-i\boldsymbol{Q}\cdot\boldsymbol{R}_{j}(0)\right) \exp(i\boldsymbol{Q}\cdot\boldsymbol{R}_j(t))\rangle \exp(-i\omega t)dt. \tag{5.14}$$

The first term on the right-hand side of Equation 5.14 describes coherent scattering, i.e. the correlation of both the same and different nuclei at different times. Hence, coherent scattering gives information about the collective dynamics in a sample. The coherent cross section is expressed in terms of scattering length as

$$\sigma_{\text{coh}} = 4\pi(\overline{b})^2. \tag{5.15}$$

The second term on the right-hand side of Equation 5.14 is incoherent scattering, i.e. the correlation between the positions of the same nucleus at different times. Thus, the incoherent scattering gives information about self motion with the cross section

$$\sigma_{\text{inc}} = 4\pi(\overline{b^2} - (\overline{b})^2). \tag{5.16}$$

If the energy is expressed as $E = \hbar\omega$ and the expressions for the cross sections are used, Equation 5.14 can be written as

$$\frac{d^2\sigma}{d\Omega\omega} = \frac{k_s}{k_i}\left(\frac{\sigma_{\text{coh}}}{4\pi}S_{\text{coh}}(Q,\omega) + \frac{\sigma_{\text{inc}}}{4\pi}S_{\text{inc}}(Q,\omega)\right). \tag{5.17}$$

where S_{coh} and S_{inc} are the coherent and incoherent structure factors, respectively. The coherent structure factor contains information about collective dynamics while the incoherent structure factor contains information about the self motion, e.g. self diffusion [100]. From Equation 5.17 it can also be found that the cross sections σ_{coh} and σ_{inc} determine the amount of coherent and incoherent scattering. For samples with large incoherent cross sections, like hydrogen rich materials, the incoherent scattering will dominate the signal. The cross section can be controlled to a certain extent by isotope substitution to increase or decrease the incoherent/coherent scattering to suit the purpose of the experiment.

A schematic of a QENS experiment is shown in Figure 5.10. An incoming neutron is scattered by the sample and registered by one of several detectors. Each detector covers a certain angle, i.e. a certain q-value, and the energy

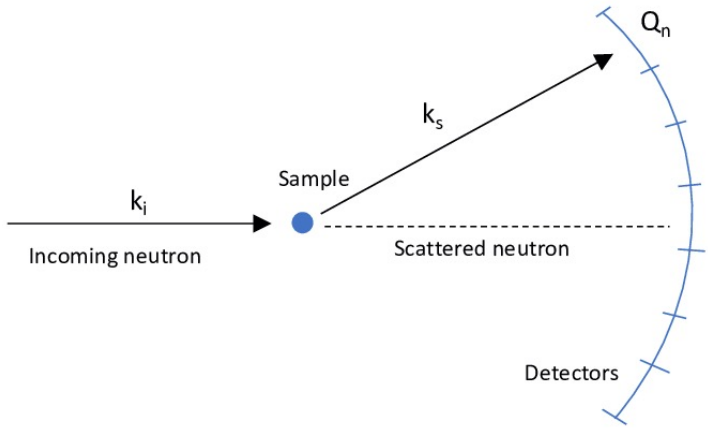

Figure 5.10: Schematic of a quasi-elastic neutron scattering experiment

of the neutron can be determined (read more about how this is done for the different techniques in section 5.4.1, 5.4.2 and 5.4.3) [100]. Thus, each detector measures the double differential cross section described in Equation 5.12.

Figure 5.11 (left) shows an example of spectra of an acetonitrile based highly concentrated electrolyte in frequency space where the intensity is shown as a function of energy transfer. The broadening of the spectrum with respect to the resolution function reflects the dynamics in the material. An increased broadening is a result of faster relaxations, e.g. as in this case the result of a lower salt concentration and a lower viscosity as shown in Figure 5.11. The data can also be presented in the time-space, in the shape of the intermediate scattering function, $I(Q,t)$, as in Figure 5.11 (right). The intermediate scattering function is related to the scattering function as

$$S(Q,\omega) = \frac{1}{2\pi}\int_{-\infty}^{\infty} I(Q,t)e^{-i\omega t}dt. \tag{5.18}$$

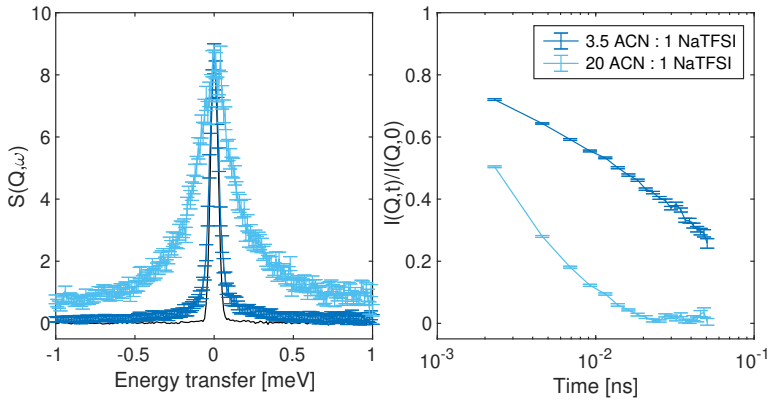

Figure 5.11: QENS data recorded at FOCUS of NaTFSI in Acetonitrile for two different concentrations measured at Q=0.95 Å^{-1}, presented in the frequency space, as S(Q,ω) (left) and in the time space, as I(Q,t) (right). The black line shows the instrument resolution.

5.4.1 Time-of-Flight Spectroscopy

IN5 at Institut Laue-Langevin (ILL), Grenoble, France [102] and FOCUS at Paul Scherrer Institute (PSI), Villigen, Switzerland [103] are two direct geometry Time-of-Flight (TOF) spectrometers that were used in this thesis. Time of flight instruments measures S(Q,ω) with an accessible timescale of $10^{-10} - 10^{-14}$ s depending on the instrument settings. Hence, TOF spectrometers are well suited to measure local dynamics in liquids such as electrolytes and ionic liquids.

Figure 5.12 shows a schematic drawing of a direct geometry time of flight instrument. From an incoming white beam a band of wavelengths is selected by the help of choppers. These are rotating disks made out of a neutron absorbing material with slits allowing for only certain wavelengths to go through. The smaller the wavelength band the higher resolution. By chopping the beam a pulse with a certain wavelength i.e., a certain velocity, and well defined starting time is created. The time of flight for the neutron from the chopper to the detector via the sample is then measured. In the scattering event the neutron either loses some (or all) of its energy or gains energy causing it to travel faster or slower than before the scattering event. From the measured time of flight of the neutron the change in energy is calculated.

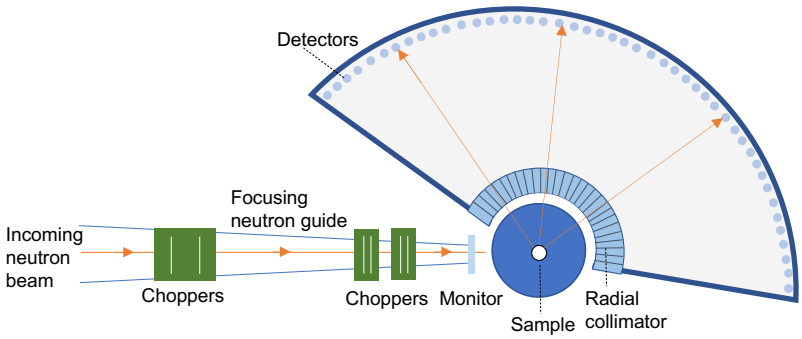

Figure 5.12: Schematic of a time of flight instrument

5.4.2 Back-Scattering Spectroscopy

The back scattering spectrometer IN16B at ILL, Grenoble, France [104] was used in this thesis to measure dynamics on the nanosecond timescale. Back scattering spectrometers have higher energy resolution than time of flight instruments and can therefore probe slower dynamics covering a timescale of $10^{-9} - 10^{-12}$ s. The high resolution implies the ability to measure smaller energy exchanges and to do so a well defined wavelength is required. Using only a small amount of the neutrons from the white beam results in a longer measuring time for back scattering instruments than for TOF instruments. Back scattering instruments measures the data in frequency space, S(Q,ω).

Figure 5.13 shows a schematic drawing of a backscattering instrument. A velocity selector and chopper are used to select neutrons in a narrow wavelength band around λ and pulse the beam. This pulse of neutrons is then directed towards the second monochromator where a 90° Bragg reflection selects a more precise selection of neutrons with wavelength λ, it is from this step back scattering has gotten its name. To induce a well defined energy spread in the neutron pulse the monochromator is positioned on a Doppler drive. Depending on the velocity of the Doppler drive at the instant the neutron is reflected in the monochromator the neutron gains or loses a small amount of kinetic energy, resulting in a well known energy distribution, E_i, of the neutrons later impinging on the sample. It is this energy distribution that determines the energy window of the instrument. Out of the scattered neutrons only the neutrons with a certain final energy E_f, determined by analysers, are directed to the detectors and counted. When a neutron with the correct energy is

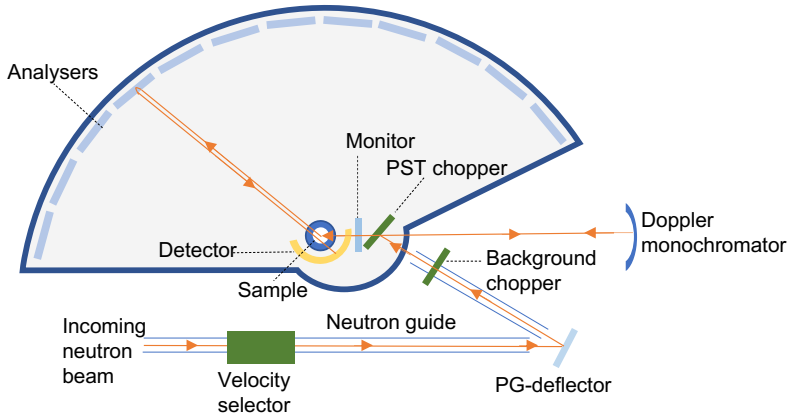

Figure 5.13: Schematic of a back scattering instrument

detected it is assigned to an energy channel by the instrument electronics. Based on the fact that the final energy is constant, the information about the velocity increase/decrease from the Doppler drive and the known distance the neutron has to travel the energy exchange in the scattering process, ΔE, can be determined.

5.4.3 Neutron Spin Echo Spectroscopy

In neutron spin echo spectroscopy the spin of the neutron is used to measure the energy exchange in the scattering event [105]. This allows for a high energy resolution, accessing a time window of $10^{-6} - 10^{-14}$ s and the dynamics are measured directly in time space, via the intermediate scattering function. In this thesis the neutron spin echo spectrometer WASP at ILL, France was used.

In neutron spin echo the individual neutrons are followed, hence there is no need for the beam to be fully monochromised, instead a broadly monochromatic beam with typically a $\Delta\lambda/\lambda$ of 10-20% is used. Figure 5.14 shows a schematic of the first neutron spin echo instrument, IN11 at ILL, Grenoble, France. The beam is polarised using a super-mirror neutron polariser. A $\pi/2$-flipper is used to rotate the spin by $\pi/2$ radians in the x-direction when travelling in the z-direction of a solenoid with a length L_1 and field strength B_1. The spin will start to Lamor precess when it enters the B-field. This can be considered

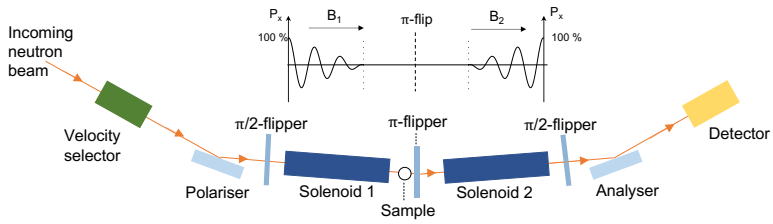

Figure 5.14: Schematic of a neutron spin echo instrument of type IN11

as starting a clock. While travelling in the solenoid the polarisation will be gradually lost as the neutrons have different velocities. After the solenoid the neutrons scatter on the sample before the spin is flipped π radians using a π-flipper, which can be considered as reversing the clock. Now with the spin in the opposite direction than previously the neutron travels through a second solenoid with a length L_2 and field strength B_2. As the spin precesses backward the initial polarisation is recovered at the end of the solenoid if the scattering event was elastic and the length and field strength of the two solenoids are the same. Then the clock is stopped and the spin is realigned to its initial direction using a second $\pi/2$-flipper.

For a quasi-elastic scattering event the velocity of the neutron is changed which will result in an unequal number of neutron precessions leading to a loss of spin polarisation [105]. If $B_1L_1 = B_2L_2$ the difference in the precession angle is described by

$$\varphi = \frac{\gamma_L B_2 L_2 \hbar\omega}{m v_1^3} = t_F \omega \tag{5.19}$$

where γ_L is the gyro-magnetic ratio of the neutron, $\hbar\omega$ the energy transfer and m and v the mass and velocity of the neutron respectively [106]. φ is proportional to ω with the proportionality constant, t_F that has the dimension time. In the quasi-elastic limit the Fourier time, t_F, is equivalent to real time [106]. The polarisation is described as the average of $cos(\omega t_F)$, which in turn is related to the intermediate scattering function

$$P(Q,t_F) = \langle cos(\omega t_F)\rangle = \int S_{\mathrm{NSE}}(Q,\omega) cos(\omega t_F) d\omega = I_{\mathrm{NSE}}(Q,t_F). \tag{5.20}$$

The time investigated, t_F, depends on the parameters of the solenoids, B and L (as seen in Equation 5.19), therefore to get more than one data point several

measurements with different settings are needed. For a full derivation of the theory, the reader is recommended to read reference [105].

5.4.4 Experimental Considerations

Often incoherent scattering is preferred in QENS experiments. This is because models for incoherent scattering are well developed while there are few models for coherent scattering [107]. Hence, QENS is particularly useful for hydrogen-rich materials that have strong incoherent signal. However, even though the incoherent signal is strong, it doesn't mean that the coherent signal is weak. This means that when the double differential cross section is measured in a QENS experiment and both the coherent and incoherent contributions are recorded the coherent scattering contribution can complicate the analysis [100]. Two methods can be used to handle this, either one chooses a sample where the incoherent signal is much larger than the coherent contribution by isotope substitution, or one uses polarised neutrons to separate the coherent and incoherent contributions [101]. There are only few instruments where polarisation is used.

The best choice of spectrometer for an experiment depends on what motion should be investigated. For faster dynamics, like the rotation of a methyl group, a time of flight spectrometer might be the best option while for slower dynamics like long-range diffusion in an ionic liquid a back scattering spectrometer is better. However, it is not only the time window of the instrument that determines what motions are studied in the experiment, also the temperature plays a big part. The motion can be slowed down or sped up to match the time window of the instrument by changing the temperature.

The sample cell is preferably an annular cylinder, if practically possible. A cylindrical geometry simplifies corrections related to absorption and multiple scattering. An alternative is to use a flat plate geometry that is more suitable for highly viscous samples and solids. However, for a flat geometry the contribution from the sample cell to the total signal will vary with the scattering angle and for highly absorbing materials the signal at angles parallel to the cell will be heavily reduced.

The thickness of the sample is typically chosen to give 90% transmission, to minimise multiple scattering. The transmitted intensity a distance z into the material follows

$$I_z \propto e^{-\sigma n z} \tag{5.21}$$

where σ is the total cross section (scattering and absorption) and n is the number density [100], and the transmission T is

$$T = \frac{I_z}{I_0} = e^{-\sigma n z}. \tag{5.22}$$

For a 90% transmission we get the thickness as a function of scattering length and number density as

$$z = -\frac{\ln(0.9)}{\sigma n} \tag{5.23}$$

5.4.5 Data reduction

Several measurements in addition to the actual sample are needed to perform a full data reduction; an empty cell measurement, a resolution measurement and a measurement of a purely elastically scattering sample. Data reduction of neutron scattering data is highly dependent on the instrument and is in general performed with software provided by the facilities, such as LAMP [108], DAVE [109] and Mantid [110], where the geometry and information from the instrument are already implemented. Initially, all data has to be normalised to the incoming beam that is measured by a monitor placed in front of the sample. The signal from the empty cell can then be subtracted. The empty cell data should ideally be recorded at the same temperature as the sample for proper background subtraction. Self-shielding and self-absorption of the sample have to be taken into account and are calculated by the reduction software based on the sample cell geometry and density of the sample and its absorption and scattering cross sections. The efficiency of the detectors of an instrument can vary and a calibration is needed to make sure the angle dependence is correctly reproduced. For this an elastically and isotropically scattering material, often vanadium, that should have the same measured intensity in all detectors is used. Finally, a resolution measurement is needed. For resolution there are two options. Either a measurement of the sample at low temperature where all motions are frozen or a measurement of vanadium or any other element that scatters purely elastically can be used, thus a vanadium sample can be used for both the resolution and the detector efficiency calibration. The advantage of using the sample at low temperature for resolution rather than vanadium is to eliminate any uncertainty of geometrical mis-match of the sample and the vanadium. After all these corrections are taken care of the conversion to S(Q,ω) or I(Q,t) can be done.

5.4.6 Data analysis

QENS data can be analysed in either frequency space, S(Q,ω), or time domain, I(Q,t). Which one to use often comes down to individual preferences, however in some situations the intermediate scattering function is advantageous. Data from neutron spin echo experiments for example are measured directly in I(Q,t) and is always analysed in the time space since the conversion from I(Q,t) to S(Q,ω) is not recommended. Using I(Q,t), data from different instruments can be combined to cover a wider time window, provided that the data is collected at the same momentum transfer. The following sections will mostly cover the analysis in frequency space with additional information about the analysis in the time domain in the end.

In a QENS experiment the measured signal not only contains the S(Q,ω) but will also have a contribution from the resolution of the instrument and a background that needs to be taken into account [111],

$$S_{\text{measured}}(Q,\omega) = (S_{\text{inc}}(Q,\omega) \otimes R(Q,\omega)) + BG \tag{5.24}$$

where R(Q,ω) is the resolution function of the instrument and $\otimes$ is the convolution operator and BG is background. Treating the data using the intermediate scattering function, I(Q,t), the convolution is transformed into a multiplication, which simplifies the separation of the resolution function and therefore the fitting of the data [106].

For strong incoherent scatterers the dynamic structure factor S(Q,ω) can be approximated as

$$S(Q,\omega) \approx S_{\text{inc}}(Q,\omega). \tag{5.25}$$

$S_{\text{inc}}(Q,\omega)$ consists of both an elastic and a quasi-elastic contribution. From the definition of the structure factor, the elastic contribution can be described by a delta function convoluted with the resolution function. The quasi-elastic contribution in case of a simple exponential relaxation in time domain, such as free diffusion, is described by a Lorentzian function in frequency space [106]. For multiple, in time well separated simple motions, the dynamical structure factor can be modelled as

$$S_{\text{inc}(Q,\omega)} = A_0(Q)\delta(\omega) + \sum_i A_i L_i(Q,\omega), \tag{5.26}$$

where A_i is the area of the functions and the Lorentzian functions are described as

$$L_i(Q,\omega) = \frac{1}{\pi}\frac{\Gamma_i(Q)}{(\hbar\omega)^2 + \Gamma_i(Q)^2}. \tag{5.27}$$

where Γ is the half width at half maximum. This approach is valid for simple exponential relaxation processes that are independent and well separated in time, otherwise more complicated models are needed. Figure 5.15 shows an example of fitted QENS data. The data was recorded at the Time-of-Flight spectrometer IN5 at ILL and is here visualised in frequency space as the measured intensity for a specific Q-value as a function of energy transfer. The data has been fitted with a resolution function, a linear background and two Lorentzian functions. Thus, here we assume that there are two relaxation processes in the material in the investigated time scale. The information about the relaxation time and the nature of the relaxations are found in the momentum transfer dependence of the half width at half maximum (Γ) and the area of the Lorentzian functions.

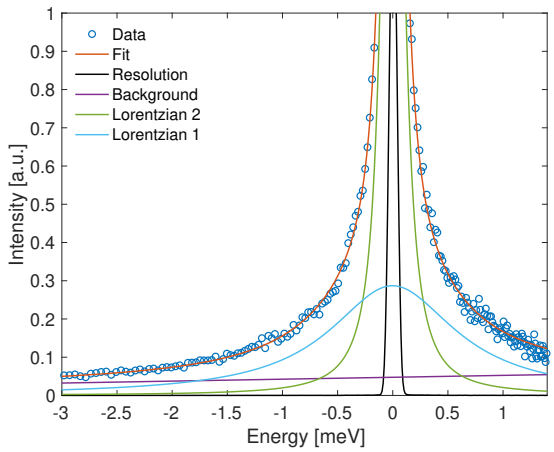

Figure 5.15: Example of fitted experimental QENS data from an acetonitrile based electrolyte with LiTFSI. Two lorentzian functions are used to fit the experimental data, as well as a delta function and a linear background.

The momentum transfer dependence of the width Γ can provide information on what type of motion the relaxations corresponds to. For liquid samples three basic models are often considered. The first model, Equation 5.28, describes a Fickian diffusion where D is the diffusion constant [112]. This is a continuous free diffusion and for small Q-values this model should be valid for all diffusion processes [113].

$$\Gamma(Q) = DQ^2. \tag{5.28}$$

Two other models describe jump diffusion with different jump length distributions. The first, the Hall-Ross model [114], assumes a Gaussian distribution of the jump length and is described in Equation 5.29 where $\langle l^2 \rangle$ is the mean jump length and τ the residence time.

$$\Gamma(Q) = \frac{1}{\tau}\left(1 - \exp(-\frac{\langle l^2 \rangle Q^2}{2})\right) \quad \text{for} \quad D = \frac{\langle l^2 \rangle}{2\tau} \tag{5.29}$$

The second model is the Teixeira model [115],

$$\Gamma(Q) = \frac{DQ^2}{1 + DQ^2\tau}, \quad \text{for} \quad D = \frac{\langle l^2 \rangle}{6\tau} \tag{5.30}$$

originally developed to describe dynamics in water, but works well also for other liquids. This model is sometimes in literature falsely attributed to Singwi and Sjölander. The Singwi-Sjölander model is also a jump diffusion model developed for liquid water [106], however a different one, which only at certain conditions reduces to the same function as the Teixeira model. Figure 5.16 shows the momentum transfer dependence of the width for the different diffusion models for comparison. The Hall-Ross and Teixeira models are plotted with a jump length $\langle l^2 \rangle$=4 Å and a residence time τ=1 ns and a simple diffusion is plotted with a diffusion coefficient of 2/3 Å^2/ps.

Local relaxations like chain rotations on molecules will show little to no Q dependence of Γ [81]. To access information of these motions the Elastic Incoherent Structure Factor (EISF) is an invaluable tool. It is defined as

$$EISF = \frac{A_{\text{elastic}}}{A_{\text{elastic}} + A_{\text{inelastic}}} \tag{5.31}$$

where A_{elastic} is the area of the elastic contribution and $A_{\text{inelastic}}$ is the area of the Lorentzian of interest. By fitting the EISF to different models one can determine what type of motion is observed and from the fitting parameters also learn about for example the geometry of the motion. Equation 5.32 describes the EISF for a methyl group rotation where j_0 is the zeroth order of the spherical Bessel function and d is the distance between the hydrogen and carbon atoms [113]. A is the fraction of signal that comes from the particular motion. For a hydrogen rich molecule it can be approximated to the ratio of hydrogen atoms taking part in the motion. For a methyl group rotation this corresponds to 3 so A will be 3 divided by the total number of hydrogen atoms

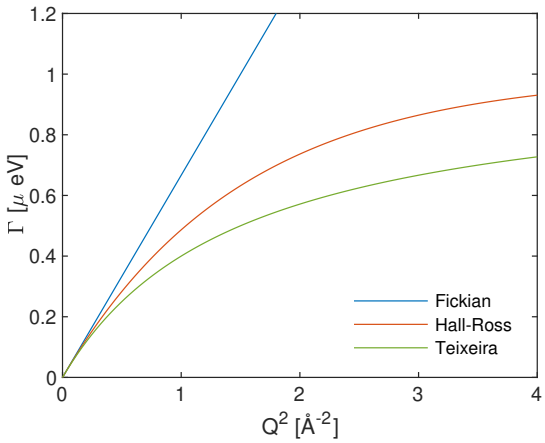

Figure 5.16: Γ as a function of Q^2 for different diffusion models, where $\langle l^2 \rangle$ was set to 4 Å and τ to 1 ns for the jump diffusions and for simple diffusion D was set to 2/3 $Å^2$/ns.

of the molecule.

$$EISF_{\text{Methyl rotation}} = (1 - A) + A\frac{1}{3}\left[1 + 2j_0\left(\sqrt{\frac{8}{3}}Qd\right)\right] \tag{5.32}$$

Another useful model is

$$EISF_{\text{Circular rotation}} = (1 - A) + A\frac{1}{N}\sum_{n=1}^{N} j_0\left[2Qr\sin\left(\frac{n\pi}{N}\right)\right] \tag{5.33}$$

that describes a random jumps on a circle of radius r with N equivalent sites [113]. For large values of N it corresponds to a continuous rotational diffusion and can be used to model the motions of alkyl chains. A third model describes a restricted diffusion inside a sphere of radius r [113].

$$EISF_{\text{Restricted diffusion}} = (1 - A) + A\left[\frac{3j_1(Qr)}{Qr}\right]^2 \tag{5.34}$$

Analysis of the EISF is used in paper I to determine the nature of two local relaxations.

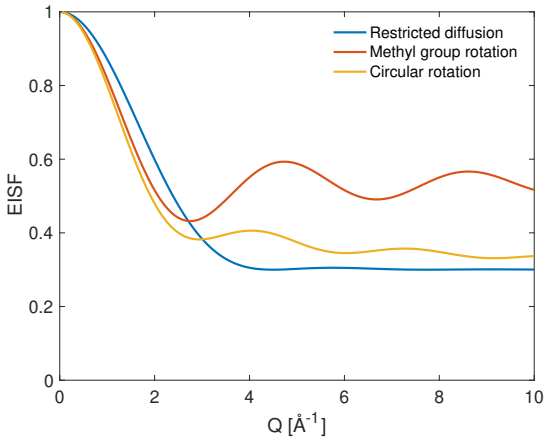

Figure 5.17: EISF for different models, where A=0.7 and r=d=1.

There are situations when one or more Lorentzian functions does not fit the data well, like for systems that exhibits a distribution of relaxation rates. Such a motion is better described in time domain using a Kohlrausch-Williams-Watt function [106]. That is a stretched exponential function (see Equation 5.35) with a stretching parameter, β, taking values between zero and one. For β=1 a simple exponential is recovered.

$$\frac{I(Q,t)}{I(Q,0)} = A\, e^{\left(-(t/\tau_{\mathrm{KWW}})^{\beta}\right)} \tag{5.35}$$

It is important to note here that τ_{KWW} is an effective relaxation time that depends on β. Instead the average relaxation time, $\langle\tau\rangle$, should be used and is calculated using

$$\langle\tau\rangle = \Gamma_G \left(\frac{1}{\beta}\right) \frac{\tau_{\mathrm{KWW}}}{\beta} \tag{5.36}$$

where Γ_G is the gamma function [106].

Chapter 6

Results

In this section the main results of the thesis are summarised. It is based on the work presented in detail in papers I-V.

6.1 Local structure in ionic liquids

Local structure in ionic liquids was investigated from various aspects, effect of temperature, pressure, type of cation/anion or effect of dilution. The results presented here are from the work in papers I, III and IV and in addition some unpublished experiments are also commented on.

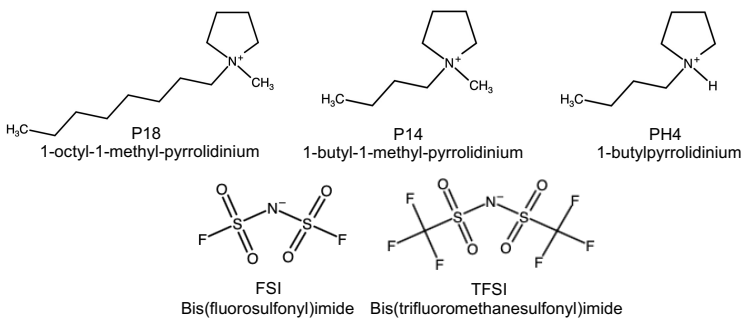

Figure 6.1: Chemical structure of anions and cations used in this thesis.

The local structure of ionic liquids was investigated using SAXS. The ionic liquids investigated all belong to the pyrrolidinium family with varying anion and cation. P14TFSI (1-Butyl-1-methylpyrrolidinium bis(trifluoromethylsulfonyl) -imide) can be considered as our starting point. The chemical structure of

P14TFSI and the other cations and anions used are found in Figure 6.1. From P14TFSI the anion is changed to the smaller anion FSI, the length of alkyl chain of the cation is increased to 8 in P18TFSI and the cation is changed for its protic counterpart in PH4TFSI. The scattering patterns are shown in Figure 6.2. The two characteristic peaks from the nearest neighbour distance, referred to as the molecular peak at Q=1.3-1.4 Å^{-1}, and the charge ordering at Q=0.8-0.9 Å^{-1} are found in all ionic liquids. The sample with longer alkyl chain, P18TFSI (1–Octyl-1-methylpyrrolidinium bis(trifluoromethylsulfonyl)imide) also shows a third peak found at Q=0.35 Å^{-1} that appears for alkyl chains (n≥6) and is the result of the formation of apolar domains [69].

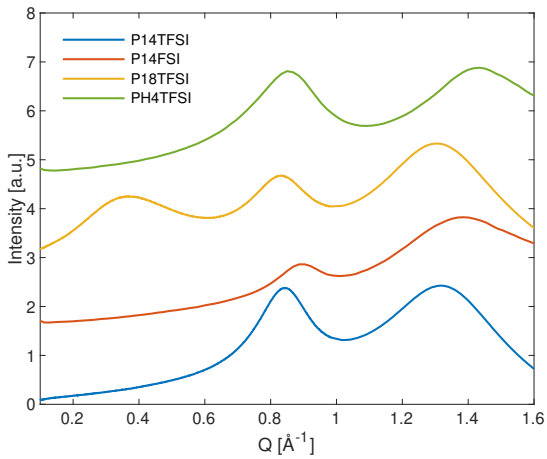

Figure 6.2: SAXS patterns for ionic liquids in the pyrrolidinium family investigated in this thesis.

From Figure 6.2 it is evident that the local structure in the different ionic liquids is very similar (apart from the pre-peak for P18TFSI) and only minor differences can be found. For P14TFSI the intensity for the two peaks are of comparable amplitude while the P14FSI (1-Butyl-1-Methylpyrrolidinium bis(fluorosulfonyl)imide) has a considerable lower intensity for the charge ordering peak, which is also shifted to larger Q. With the FSI anion being smaller than the TFSI anion it is expected that the distance between similar charges (cation-cation and anion-anion) will be smaller. Shifting the attention to the sample with longer alkyl chain, P18TFSI, the charge ordering peak shifts to slightly lower Q. The dependence of alkyl chain length on the peak position is relatively weak despite the larger size of the cation [69]. PH4TFSI

(1-Butylpyrrolidinium bis(trifluoromethylsulfonyl)imide) is a protic ionic liquid and hydrogen bonding between the ions is possible. Comparing the peak position of the charge ordering for P14TFSI and PH4TFSI we find a small shift to higher Q for PH4TFSI which can be a result of hydrogen bonding in the ionic liquid. However, the effect of potential hydrogen bonding is smaller than the effect of having a smaller anion. The molecular peak of PH4TFSI also shifts to slightly higher Q, indicating a slightly closer packing of nearest neighbours as a result of hydrogen bond interaction between cation and anion.

6.1.1 Effect of temperature and pressure

The temperature and pressure dependence of the local structure in the ionic liquid, P14TFSI, was investigated with SAXS, the result is found in Figure 6.3. With decreasing temperature and increasing pressure, both the molecular and the charge ordering peak shift to higher Q, in line with the induced increase in density. Similar temperature trends have been reported in literature [68, 116, 117]. The pressure dependence was investigated also by Pilar et al. and showed the same dependence of the molecular peak position [118], however in that study the shift of the charge ordering peak was not conclusive. In Figure 6.3c the SAXS patterns at state points of isoconductivity are compared, that is state points that all show the same conductivity. These points were chosen in order to investigate the link between the conductivity and the local structure of the ionic liquid. In the figure the peak positions of the three curves show little variation, whereas the intensity of the charge ordering peak decreases slightly at the state points with high pressure, reflecting the strong pressure dependence of the intensity of this peak, see Figure 6.3b. Thus, for state points with the same macroscopic dynamics (conductivity), the structural correlations are invariant, pointing to a strong connection between the local structure and the dynamics. This is supported by our previous study (not included in this thesis), where it was shown that the changes in the molecular peak quantitatively follow the density change [119].

6.1.2 Effect of dilution

The protic ionic liquid PH4TFSI was diluted with water and studied with SAXS to investigate the effect that added water has on the local ordering. Figure 6.4a shows the SAXS patterns of PH4TFSI and D_2O diluted PH4TFSI at room temperature. The pattern from the D_2O diluted sample shows very similar

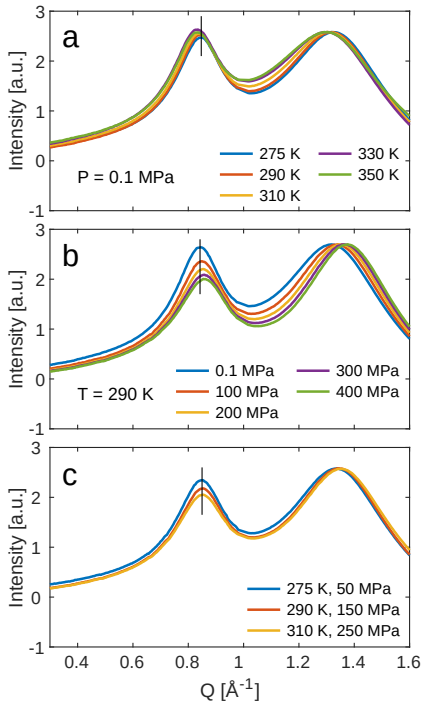

Figure 6.3: SAXS patterns for P14TFSI as a function of (a) temperature, (b) pressure and (c) isoconductivity.

features as the neat ionic liquid. This is in agreement with previous studies on an aprotic ionic liquid where no larger structural changes were found for water concentrations below 50 mol% [87]. However, there is a shift in the peak positions of both the molecular and the charge ordering peak towards smaller Q-values with the amount of water added. The shift of the molecular peak to smaller Q-values indicates an increased distance between nearest neighbours and correlates well with the decrease in the density with the addition of water reported previously for the same system [86]. Similarly the shift of the charge ordering peak to smaller Q-values implies an increase in the distance between similar charges. Yaghini et al, show that the preferential interaction site of water in the protic ionic liquid, C2HImTFSI, is the -NH group of the cation [85].

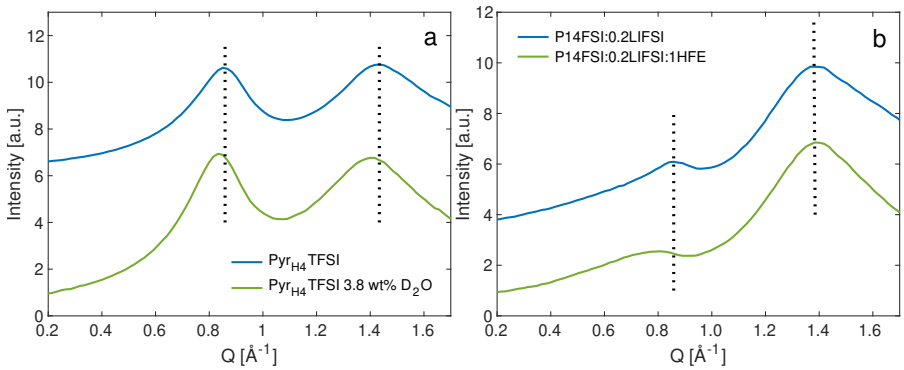

Figure 6.4: SAXS patterns of diluted ionic liquids: (a) PH4TFSI and D_2O diluted PH4TFSI, measured at room temperature. Dotted lines mark the peak positions in the SAXS pattern of the neat ionic liquid. Data has been offset vertically for clarity. (b) Ionic liquid electrolyte, P14FSI:0.2LiFSI, and HFE diluted ionic liquid electrolyte, P14FSI:0.2LiFSI:1HFE. Dotted lines mark the peak positions in the SAXS pattern of the ionic liquid electrolyte

The cation then effectively becomes larger with the water bonded to it, and therefore the distances between similar charges is expected to increase. It is found from IR-spectroscopy that the system investigated here show a similar behaviour, with water preferentially hydrogen bonding to the pyrrolidinium ring on the cation. However, IR-data also indicate that water is not fully dispersed and smaller clusters of water molecules also exist. This supports the findings from MD-simulations on water mixtures with PH4TFSI which suggest the presence of small clusters of water, from a few water molecules bridging between anion and cation of the ionic liquid to aggregates of around 10 molecules dispersed in the ionic matrix [86].

The effect on the local structure of dilution using a hydrofluoroether, 1,1,2,2-Tetrafluoroethyl 2,2,2-Trifluoroethyl Ether (HFE), in an ionic liquid electrolyte was also investigated using SAXS. P14FSI and LiFSI was mixed to form the ionic liquid electrolyte. From Raman measurements Li-FSI clusters are formed in this electrolyte with an average of 2 FSI molecules interacting with each Li^+. These clusters form larger effective anions and are important for the performance of the ionic liquid electrolyte, hence, the diluent should preferably not disrupt this structure. Adding HFE to the ionic liquid electrolyte shifted the charge ordering peak to lower Q-values as seen in Figure 6.4b. This shows

that HFE somewhat influences the nano-scale structure of the IL-electrolyte causing a further separation of similar charges, similarly to the effect of adding water to the protic ionic liquid but with a stronger effect due to the larger size of HFE compared to water. A scenario that is compatible with this observation is that HFE does not interact with the Li[FSI]x clusters but preferentially associates with the P14 cation of the ionic liquid and in this way effectively increases the length scale of charge ordering. Indeed, from Raman spectroscopy it is found that the addition of HFE has only a very slight effect on the band positions and the average coordination number of FSI per Li^+. Thus, this shows that the HFE does not interrupt the solvation structure of Li-ions, but dilutes the electrolyte while maintaining the favourable structure of the ionic liquids.

6.2 Local dynamics in ionic liquids

Local dynamics in ionic liquids was investigated using different QENS spectrometers. The effect of temperature, pressure, type of cation/anion and the effect of dilution of the ionic liquid was studied. The results presented here are from the work in papers I, III and IV and in addition some unpublished experiments are also commented on.

In ionic liquids there are microscopic dynamics such as librations of the pyrrolidinium ring of the cation and rotations of side chains of the cation on the time scale of picoseconds. On longer time scales, around nanoseconds the dynamics is typically of a more diffusional nature. All motions can be probed using different QENS instruments, as illustrated in Figure 6.5.

Local dynamics of an aprotic ionic liquid, P14TFSI and its protic counter part, PH4TFSI was investigated using the neutron spin echo spectrometer WASP at ILL, France. Intermediate scattering functions are shown as a function of momentum transfer in Figure 6.6a. For both samples the majority of the incoherent (and total) scattering comes from the pyrrolidinium cation, hence it is the relaxation of the cation that is followed. The two ionic liquids have very similar intermediate scattering functions, indicating that the hydrogen bonding found in the protic ionic liquid has little effect on the local cation dynamics. Without fitting the data, and by just observing the curves, indications of two relaxations can be seen, one faster around 10^{-2} ns and one slower around 1

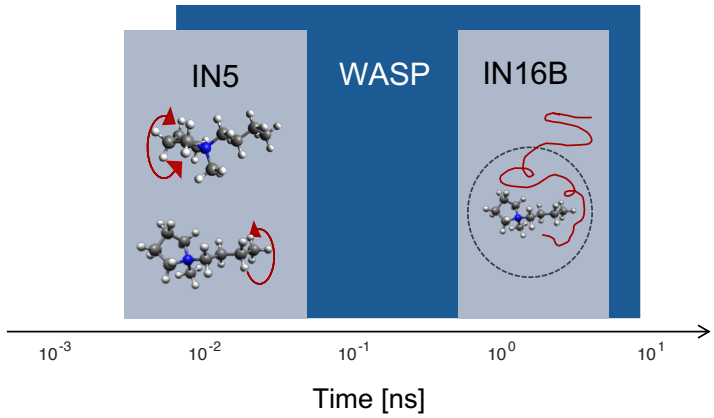

Figure 6.5: Time scales covered by the QENS instrument IN5, IN16B and WASP and examples of motions that typically occur on these time scales.

ns. The effect of the anion on the intermediate scattering function is shown in Figure 6.6b, comparing results of of P14TFSI and P14FSI at 270 K and momentum transfer Q=0.6 $Å^{-1}$. P14FSI clearly shows faster relaxation compared to P14TFSI, which in line with the higher conductivity found in P14FSI compared to P14TFSI [120]. To learn more about the various relaxations found in P14TFSI on pico- to nanosecond timescales the two spectrometers IN5 and IN16B at ILL, France were used. The time windows covered by the two instrument is seen in Figure 6.5. With IN5 faster dynamics can be investigated, typically local dynamics of the molecule like alkyl chain rotations or librational motions. IN16B is an instrument with higher energy resolution, and therefore measures slower dynamics e.g. diffusional motions.

P14TFSI shows dynamics in both time windows, as expected from the intermediate scattering function measured on WASP (Figure 6.6a). At short time scales, two processes are revealed from experiments at IN5. The data from IN5 was analysed in the frequency domain where the broadening of the quasi-elastic component is related to the time scale of the dynamics. The broadening is found to be independent of momentum transfer for both processes which indicates that these motions are of a local origin [81]. Analysis of the momentum transfer dependence of the elastic incoherent structure factor suggests that the two processes are a librational motion of the carbon ring of

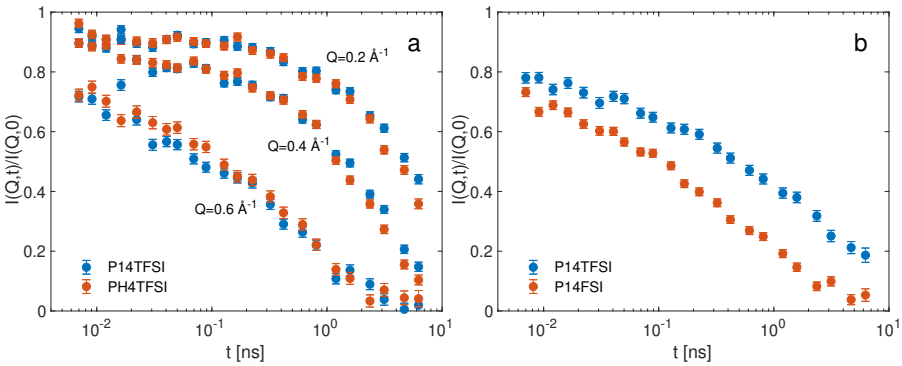

Figure 6.6: Intermediate scattering functions of (a) P14TFSI and PH4TFSI at 300 K as a function of momentum transfer, (b) P14TFSI and P14FSI at 270 K and Q=0.6 Å^{-1}. The data was collected using the WASP spectrometer at ILL, France.

the cation and conformational change, of the butyl side chain of the cation. These motions show little to no temperature dependence and are therefore believed to be separated from the conductivity. The IN16B data reveals a confined translational diffusion on longer time scales. The confinement is believed to be about 4-5 Å and corresponds well to the charge ordering in the liquid. The size of the confinement increases with temperature and decreases with pressure, which is in line with the behaviour of the charge ordering seen from the SAXS-studies. For temperature and pressure points with constant conductivity the size of the confinement is found to be invariant, this is also the case for the diffusion coefficients determined from the neutron data. From these results it could be assumed that the conductivity is controlled by this confined translational diffusion. An illustration of the local dynamics found in P14TFSI is shown in Figure 6.5.

The choice of neutron spectrometer will play a big role in what motions that can be distinguished. Looking back at the intermediate scattering function measured of P14TFSI with the WASP spectrometer shown in Figures 6.6a and 6.6b, a larger time window than what IN5 and IN16B combined cover is achieved in one setting. Still, it only show signs of two relaxation due to that it does not truly cover the faster time scales and that the resolution in time is lower, whereas the detailed investigations using the two instruments IN5 and IN16B show that in fact three relaxations can be distinguished.

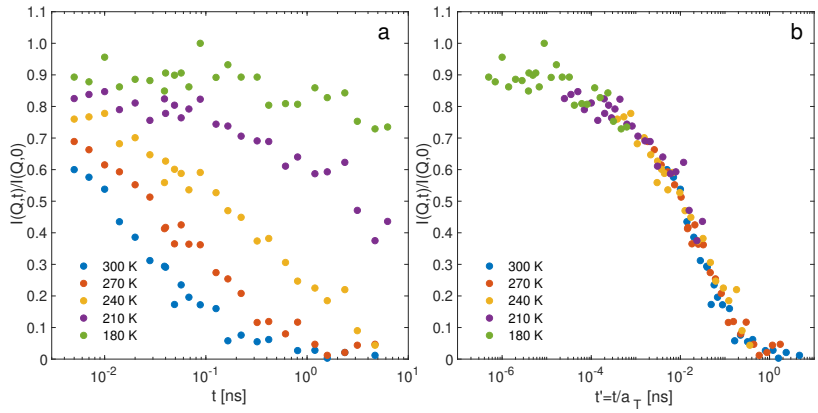

Figure 6.7: Intermediate scattering of P14FSI:0.2LiFSI:1HFE at Q=0.8 $Å^{-1}$ (a) as a function of temperature (b) time temperature superpositioned

6.2.1 Effect of dilution on local dynamics in ionic liquids

The influence of the addition of HFE, on the local dynamics in an ionic liquid electrolyte was studied with neutron spin echo using the WASP spectrometer covering timescales of $\sim$ 6 ps to 6 ns. In the experiment incoherent scattering dominates and the majority originates from the P14 cation, hence, the dynamics of P14 is probed. The main relaxation has a strong Q-dependence indicative of a diffusional motion. Time-temperature superposition was used to create a master curve showing the full relaxation of the sample (see Figure 6.7). The TTS curve shows that the shape of the intermediate scattering function is temperature independent. A stretched exponential is used to fit all concentrations indicating the the dilution does not dramatically affect the nature of the dynamics. The stretching parameter β is rather low (0.4) which indicate that the dynamics is heterogenous, i.e. a distribution of relaxation times, or of a more cooperative nature [106].

The incoherent relaxation shows a crossover in the Q-dependence around 1 $Å^{-1}$, see figure 6.8. At larger Q-values a Fickian diffusion behaviour is seen while for lower Q-values a stronger Q-dependence than predicted by Fickian diffusion is found ($>Q^2$). The average relaxation time, $< \tau >$ is scaled with Q^2 to easier detect deviations from the Fickian behaviour. This type of crossover behaviour in the dynamics with momentum transfer has also been reported for

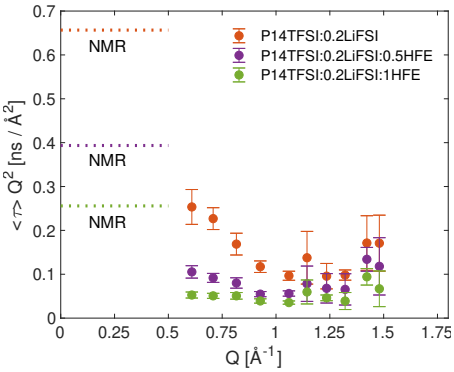

Figure 6.8: Momentum transfer dependence of average relaxation time multiplied with Q^2 for P14FSI:0.2LiFSI as a function of HFE concentration at 300 K.

a neat ionic liquid, where it was attributed to a transition from Gaussian to non-Gaussian behaviour [121]. In figure 6.8 the relaxation time corresponding to the macroscopic diffusion coefficient measured by NMR for the IL cation is indicated and it can be noted that the dynamics measured with QENS is faster than what is extrapolated from the self-diffusion coefficient.

6.3 Structure in highly concentrated electrolytes

Acetonitrile based highly concentrated electrolytes with both LiTFSI (lithium bis(fluorosulfonyl)imide) and NaTFSI (sodium bis(fluorosulfonyl)imide) (LiTFSI:xACN and NaTFSI:xACN) have been investigated to find how the structure and dynamics develops as a function of concentration, and the significance of the choice of cation. The results presented here are from the work in papers II and V and in addition some unpublished experiments are also commented on.

Acetonitrile has only one broad peak in the structure factor measured by SAXS, the nearest neighbour peak, Figure 6.9a. From fitting of the peak it is evident that it is in fact two close adjacent peaks, corresponding to parallel and anti-parallel nearest neighbour ordering of acetonitrile molecules. As salt

is added, a second peak appears at lower Q-values. It increases in intensity and moves to higher Q with increasing salt concentration. At the highest concentration this peak occurs around the same position as the charge ordering peak found in ionic liquids, see comparison in Figure 6.9b.

The origin of the low Q peak can be a result of correlations between the solvation cluster of Li^+, hence when the solvation shells are in contact with each other at high concentrations the position of the low Q peak can be is used to estimate the size of the solvation shells. It is observed the that the peak is consistently found at lower Q-values for NaTFSI:xACN. This points to that the charge correlation, or size of the solvation shells, is larger in the sodium salt electrolyte compared to the lithium salt electrolyte. This is in agreement with results from AIMD simulations which showed larger solvation shells in $NaPF_6$/acetonitrile electrolytes compared to the $LiPF_6$ analogues [49].

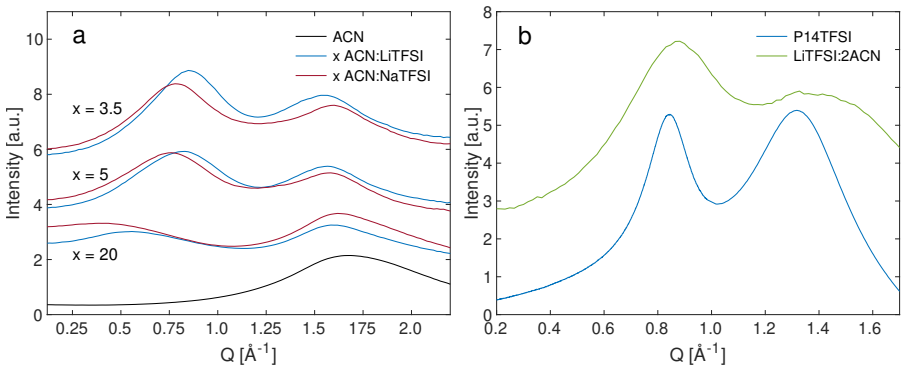

Figure 6.9: SAXS patterns for (a) acetonitrile-based electrolytes at different LiTFSI (blue) and NaTFSI (red) concentrations. SAXS pattern for neat ACN is added for comparison. (b) Scattering patterns of LiTFSI:2ACN and the ionic liquid P14TFSI. Data has been shifted vertically for clarity.

6.4 Dynamics in highly concentrated electrolytes

Local dynamics in highly concentrated electrolytes was investigated using different QENS spectrometers. The impact of temperature, salt concentration and cation on the local dynamics is presented. The results presented here are from the work in papers II and V.

Acetonitrile based electrolytes with varying concentrations of LiTFSI, were studied using QENS on IN16B at ILL, France. With increasing salt concentration the dynamic becomes progressively slower. For the lower concentrations (20:1) the motions were too fast for the instrument and only the 5:1 and 2:1 concentrations were in the time window of the instrument. Similarly to the ionic liquids, the highly concentrated electrolytes show diffusional motions on the nanosecond time scales. This particular motion was fitted to a jump diffusion model [115] where the jump length was found to be invariant of temperature and concentration, see Figure 6.10. The residence time in between jumps, however, was found to be highly dependent on temperature and concentration where high temperatures showed a shorter residence time, and the higher concentrations a longer residence time. We can envisage this jump diffusion as a rotation, or reconfiguration, of an acetonitrile molecule or TFSI anion in the solvation shell, which would correspond to a dissociation from a particular Li^+. Deuterated acetonitrile that contributed similarly as TFSI to the scattering cross section was used in this experiment, hence the signal is a combination of the two.

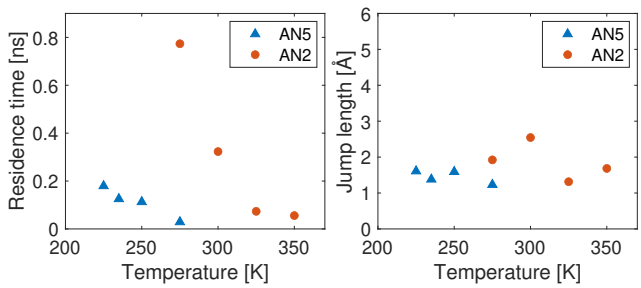

Figure 6.10: Residence time and jump length found in acetonitrile/LiTFSI highly concentrated electrolytes.

To investigate the effect of the cation LiTFSI:3.5ACN and NaTFSI:3.5ACN were studied using the FOCUS spectrometer at PSI, Switzerland. This spectrometer covers a time window of $\sim$ 3 ps - 30 ps, considerable faster than IN16B. The data was Fourier transformed to the intermediate scattering function and fitted with a stretched exponential. The Q-dependence of $1/<\tau>$ is seen in Figure 6.11a. At low Q a linear dependence, typical for a Fickian diffusion, was found and could be used to calculate diffusion coefficients for the two electrolytes. The scattering is dominated by the inocherent scattering from

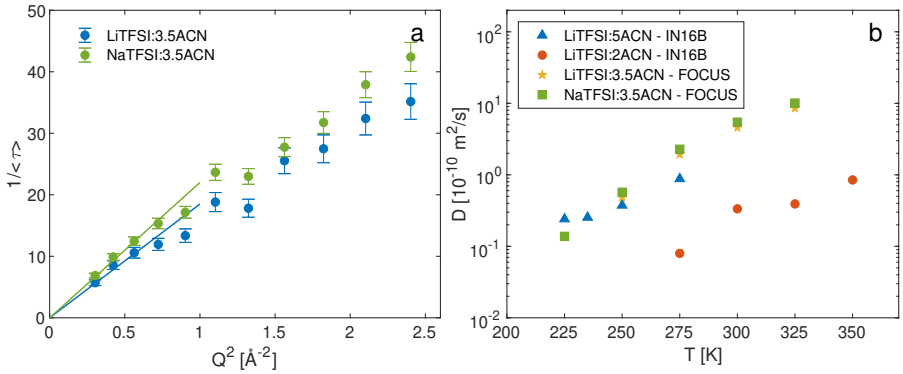

Figure 6.11: Momentum transfer dependence of the inverse relaxation time of LiTFSI:3.5ACN and NaTFSI:3.5ACN measured at 275 K. The line at low Q is a guide to the eye. (b) Diffusion coefficients of highly concentrated acetonitrile electrolytes measured by QENS at the spectrometers IN16B and FOCUS.

the acetonitrile, hence it is the diffusion of acetonitrile that is probed here. The diffusion coefficients are shown in Figure 6.11b together with the diffusion coefficients obtained from the jump diffusion model of the data recorded on IN16B. The diffusion coefficient measured for LiTFSI:3.5ACN on FOCUS is higher than both LiTFSI:2ACN and LiTFSI:5ACN from IN16B, indicating that it is different motions that are probed with the two instruments. For this faster relaxation probed with the FOCUS instrument the NaTFSI-electrolyte shows slightly faster dynamics of the acetonitrile molecule compared to the LiTFSI analogue. One should note that in the IN16B experiment deuterated acetonitrile was used and there is a significant contribution to the signal also from the anion, which can also explain the difference between the two experiments.

Chapter 7

Summary and Outlook

For the realisation of next generation battery concepts the development of the electrolyte is vital. In this thesis much effort was invested in understanding the local structure and dynamics in the two promising electrolyte concepts, ionic liquids and highly concentrated electrolytes. Several techniques have been used to cover both microscopic and macroscopic properties.

Ionic liquids were investigated using several neutron spectrometers to determine what local dynamics where present and if these dynamics contribute to the conductivity. It was found that the conductivity was strongly linked to a diffusion process confined within a cage of the nearest neighbours.

To lower the viscosity of an ionic liquid electrolyte it was diluted with HFE. The HFE was predicted to not interact with lithium and indeed, was found to preferably interact with the ionic liquid cation rather than the Li-FSI_2 triplets. While the addition of HFE increased the conductivity and resulted in faster local dynamics it did not alter the nature of the motion on the microscopic scale. Similarly to the HFE diluted ionic liquid electrolyte when added water to a protic ionic liquid the nature of the local dynamics was preserved. A preferred hydrogen bonding between the water and the cation but also the formation of small water clusters was found.

By comparing two highly concentrated electrolytes with Na- and Li-salt, it was experimentally shown that the sodium ion have a larger solvation shell than lithium and that the local diffusion is faster in the sodium electrolyte. Looking closer into the diffusion mechanism in the highly concentrated Li-salt electrolyte a jump diffusion in and out of the solvation shell was found and predicted to be a part of the ion transport mechanism in these highly concentrated electrolytes.

Today there are many promising concepts for new electrolytes but there is still a lack of fundamental understanding of the ion transport mechanism

and structure in these electrolytes. In this thesis the fundamental properties are investigated not only for basic understanding of effects like temperature and pressure but also for applied research. The experiment on diluted highly concentrated electrolytes connect directly to the work of our group to develop electrolytes for metal anodes.

The local dynamics is these systems are found to span over several order of decades. Therefore, to probe the full relaxation function a combination of instruments, or a spectrometer with a wide time window and wide momentum transfer range like WASP should be used. WASP is unique in its design and an excellent example of how instrument development has provided better conditions for studies of local dynamics.

For further studies of the dynamics in systems like those investigated here the use of polarised neutrons is recommended. It allows for a true separation of incoherent and coherent scattering without deuteration. Whereas the technique today is limited by a low flux of polarised neutrons, hopefully within a few years the technique will be available for use at the European Spallation Source, ESS.

Acknowledgements

Thank you...

- Aleks - I am truly thankful for having you as my supervisor. I don't think I could have had a better one. Well, I guess that would have been that guy that actually won supervisor of the year... Jokes a side, if I got to decide you would win every year.
- Patrik - My examiner and fellow Smålänning, thank you for these years.
- Marianne - My awesome co-supervisor. You are my role model.
- Swedness - Thank you for funding my research and providing me with courses, visits and a great group of colleagues and friends.
- Elin & Karolina - You are the best thing Swedness gave me (even better than the Yasuragi spa!).
- Matthew - My PhD twin (although you somehow grew up six months faster than me!) These five years would have been nothing without you. You make everyday at work a little better.
- Linnea - My work-bestie! Talking with you always makes things seem more manageable. I'm so happy I have someone like you that makes my messy desk look less messy.
- Adrian - Thanks for all these years in the best office, and especially for these last few months of thesis writing. It has been great to have some company, and such a great company as well!
- (K)MF - Through all my years at (K)MF, I've always thought that I had the best workplace and the best colleagues. This, despite that everyone that worked here when I started have been replaced. I leave my legacy of the Fikalist and fitness-challenge in your hands now.
- Family & Friends - I am so happy to have you in my life, all of you.
- Andreas - My fiancé. Your support (and lunchboxes) has meant the world to me. I wouldn't have managed this without you. ♡

Bibliography

[1] T Nagaura and K Tozawa. Progress in batteries and solar cells. *JEC Press*, 9:209, 1990.

[2] Amer Hammami, Nathalie Raymond, and Michel Armand. Lithium-ion batteries: runaway risk of forming toxic compounds. *Nature*, 424(6949):635–636, aug 2003.

[3] Daniel T Hallinan and Nitash P Balsara. Polymer Electrolytes. *Annual Review of Materials Research*, 43(1):503–525, jul 2013.

[4] Arumugam Manthiram, Xingwen Yu, and Shaofei Wang. Lithium battery chemistries enabled by solid-state electrolytes. *Nature Reviews Materials*, 2(4):16103, 2017.

[5] Jürgen Janek and Wolfgang Zeier. A solid future for battery development. *Nature Energy*, 1:16141, sep 2016.

[6] Yuki Yamada and Atsuo Yamada. Review—superconcentrated electrolytes for lithium batteries. *Journal of The Electrochemical Society*, 162(14):A2406–A2423, 2015.

[7] Jianming Zheng, Joshua A Lochala, Alexander Kwok, Zhiqun Daniel Deng, and Jie Xiao. Research Progress towards Understanding the Unique Interfaces between Concentrated Electrolytes and Electrodes for Energy Storage Applications. *Advanced Science*, 4(8):1700032, aug 2017.

[8] Masayoshi Watanabe, Morgan L Thomas, Shiguo Zhang, Kazuhide Ueno, Tomohiro Yasuda, and Kaoru Dokko. Application of Ionic Liquids to Energy Storage and Conversion Materials and Devices. *Chemical Reviews*, 117(10):7190–7239, may 2017.

[9] Xin Zhang, Yongan Yang, and Zhen Zhou. Towards practical lithium-metal anodes. *Chemical Society Reviews*, 49(10):3040–3071, 2020.

[10] Yuki Yamada, Jianhui Wang, Seongjae Ko, Eriko Watanabe, and Atsuo Yamada. Advances and issues in developing salt-concentrated battery electrolytes. *Nature Energy*, 4(4):269–280, 2019.

[11] Robert Hayes, Gregory G. Warr, and Rob Atkin. Structure and nanostructure in ionic liquids. *Chemical Reviews*, 115(13):6357–6426, 07 2015.

[12] Xia Cao, Hao Jia, Wu Xu, and Ji-Guang Zhang. Review—localized high-concentration electrolytes for lithium batteries. *Journal of The Electrochemical Society*, 168(1):010522, jan 2021.

[13] Yuichi Aihara, Kyoko Sugimoto, William S Price, and Kikuko Hayamizu. Ionic conduction and self-diffusion near infinitesimal concentration in lithium salt-organic solvent electrolytes. *The Journal of Chemical Physics*, 113(5):1981–1991, jul 2000.

[14] Yuki Yamada and Atsuo Yamada. Review—Superconcentrated Electrolytes for Lithium Batteries. *Journal of The Electrochemical Society*, 162(14):A2406–A2423, 2015.

[15] John B. Goodenough and Youngsik Kim. Challenges for rechargeable li batteries. *Chemistry of Materials*, 22(3):587–603, 2010.

[16] Y. Wu. *Lithium-Ion Batteries: Fundamentals and Applications*. Electrochemical Energy Storage and Conversion. CRC Press, 2015.

[17] Buket Boz, Tanmay Dev, Alberto Salvadori, and Jennifer L. Schaefer. Review—electrolyte and electrode designs for enhanced ion transport properties to enable high performance lithium batteries. *Journal of The Electrochemical Society*, 168(9):090501, sep 2021.

[18] Kang Xu. Nonaqueous Liquid Electrolytes for Lithium-Based Rechargeable Batteries. *Chemical Reviews*, 104(10):4303–4418, oct 2004.

[19] Johan Scheers, Sébastien Fantini, and Patrik Johansson. A review of electrolytes for lithium–sulphur batteries. *Journal of Power Sources*, 255:204–218, 2014.

[20] Catia Arbizzani, Giulio Gabrielli, and Marina Mastragostino. Thermal stability and flammability of electrolytes for lithium-ion batteries. *Journal of Power Sources*, 196(10):4801–4805, 2011.

[21] Tetsuya Kawamura, Arihisa Kimura, Minato Egashira, Shigeto Okada, and Jun-Ichi Yamaki. Thermal stability of alkyl carbonate mixed-solvent electrolytes for lithium ion cells. *Journal of Power Sources*, 104(2):260–264, 2002.

[22] Gerardine G Botte, Ralph E White, and Zhengming Zhang. Thermal stability of LiPF6–EC:EMC electrolyte for lithium ion batteries. *Journal of Power Sources*, 97-98:570–575, 2001.

[23] K Karuppasamy, Jayaraman Theerthagiri, Dhanasekaran Vikraman, Chang-Joo Yim, Sajjad Hussain, Ramakant Sharma, Thandavaryan Maiyalagan, Jiaqian Qin, and Hyun-Seok Kim. Ionic Liquid-Based Electrolytes for Energy Storage Devices: A Brief Review on Their Limits and Applications. *Polymers*, 12(4):918, apr 2020.

[24] Kang Xu, Yiufai Lam, Sheng S Zhang, T Richard Jow, and Timothy B Curtis. Solvation Sheath of Li+ in Nonaqueous Electrolytes and Its Implication of Graphite/Electrolyte Interface Chemistry. *The Journal of Physical Chemistry C*, 111(20):7411–7421, may 2007.

[25] Kang Xu. "charge-transfer" process at graphite/electrolyte interface and the solvation sheath structure of li+ in nonaqueous electrolytes. *Journal of The Electrochemical Society*, 154(3):A162, 2007.

[26] Zhen-Kun Tang, John S Tse, and Li-Min Liu. Unusual Li-Ion Transfer Mechanism in Liquid Electrolytes: A First-Principles Study. *The Journal of Physical Chemistry Letters*, 7(22):4795–4801, nov 2016.

[27] Masaki Okoshi, Chien-Pin Chou, and Hiromi Nakai. Theoretical Analysis of Carrier Ion Diffusion in Superconcentrated Electrolyte Solutions for Sodium-Ion Batteries. *The Journal of Physical Chemistry B*, 122(9):2600–2609, mar 2018.

[28] Oleg Borodin, Liumin Suo, Mallory Gobet, Xiaoming Ren, Fei Wang, Antonio Faraone, Jing Peng, Marco Olguin, Marshall Schroeder, Michael S Ding, Eric Gobrogge, Arthur von Wald Cresce, Stephen Munoz, Joseph A Dura, Steve Greenbaum, Chunsheng Wang, and Kang Xu. Liquid Structure with Nano-Heterogeneity Promotes Cationic Transport in Concentrated Electrolytes. *ACS Nano*, 11(10):10462–10471, oct 2017.

[29] C. Austin Angell. Dynamic processes in ionic glasses. *Chemical Reviews*, 90(3):523–542, 1990.

[30] C. A. Angell. Formation of glasses from liquids and biopolymers. *Science*, 267(5206):1924–1935, 1995.

[31] M. D. Ediger, C. A. Angell, and Sidney R. Nagel. Supercooled liquids and glasses. *The Journal of Physical Chemistry*, 100(31):13200–13212, 1996.

[32] Yuki Yamada, Yasuyuki Takazawa, Kohei Miyazaki, and Takeshi Abe. Electrochemical Lithium Intercalation into Graphite in Dimethyl Sulfoxide-Based Electrolytes: Effect of Solvation Structure of Lithium Ion. *The Journal of Physical Chemistry C*, 114(26):11680–11685, jul 2010.

[33] Liumin Suo, Oleg Borodin, Tao Gao, Marco Olguin, Janet Ho, Xiulin Fan, Chao Luo, Chunsheng Wang, and Kang Xu. "Water-in-salt" electrolyte enables high-voltage aqueous lithium-ion chemistries. *Science*, 350(6263):938 LP – 943, nov 2015.

[34] Soon-Ki Jeong, Hee-Young Seo, Dong-Hak Kim, Hyun-Kak Han, Jin-Gul Kim, Yoon Bae Lee, Yasutoshi Iriyama, Takeshi Abe, and Zempachi Ogumi. Suppression of dendritic lithium formation by using concentrated electrolyte solutions. *Electrochemistry Communications*, 10(4):635–638, 2008.

[35] Yuki Yamada, Keizo Furukawa, Keitaro Sodeyama, Keisuke Kikuchi, Makoto Yaegashi, Yoshitaka Tateyama, and Atsuo Yamada. Unusual Stability of Acetonitrile-Based Superconcentrated Electrolytes for Fast-Charging Lithium-Ion Batteries. *Journal of the American Chemical Society*, 136(13):5039–5046, apr 2014.

[36] Yuki Yamada, Makoto Yaegashi, Takeshi Abe, and Atsuo Yamada. A superconcentrated ether electrolyte for fast-charging Li-ion batteries. *Chemical Communications*, 49(95):11194–11196, 2013.

[37] Kazuki Yoshida, Mizuho Tsuchiya, Naoki Tachikawa, Kaoru Dokko, and Masayoshi Watanabe. Change from Glyme Solutions to Quasi-ionic Liquids for Binary Mixtures Consisting of Lithium Bis(trifluoromethanesulfonyl)amide and Glymes. *The Journal of Physical Chemistry C*, 115(37):18384–18394, sep 2011.

[38] Dennis W. McOwen, Daniel M. Seo, Oleg Borodin, Jenel Vatamanu, Paul D. Boyle, and Wesley A. Henderson. Concentrated electrolytes: decrypting electrolyte properties and reassessing al corrosion mechanisms. *Energy Environ. Sci.*, 7:416–426, 2014.

[39] Kazuhide Ueno, Kazuki Yoshida, Mizuho Tsuchiya, Naoki Tachikawa, Kaoru Dokko, and Masayoshi Watanabe. Glyme–Lithium Salt Equimolar Molten Mixtures: Concentrated Solutions or Solvate Ionic Liquids? *The Journal of Physical Chemistry B*, 116(36):11323–11331, sep 2012.

[40] Jianhui Wang, Yuki Yamada, Keitaro Sodeyama, Ching Hua Chiang, Yoshitaka Tateyama, and Atsuo Yamada. Superconcentrated electrolytes for a high-voltage lithium-ion battery. *Nature Communications*, 7(1):12032, 2016.

[41] Arumugam Manthiram, Yongzhu Fu, Sheng-Heng Chung, Chenxi Zu, and Yu-Sheng Su. Rechargeable lithium–sulfur batteries. *Chemical Reviews*, 114(23):11751–11787, 2014. PMID: 25026475.

[42] Liumin Suo, Yong-Sheng Hu, Hong Li, Michel Armand, and Liquan Chen. A new class of Solvent-in-Salt electrolyte for high-energy rechargeable metallic lithium batteries. *Nature Communications*, 4(1):1481, 2013.

[43] Kaoru Dokko, Naoki Tachikawa, Kento Yamauchi, Mizuho Tsuchiya, Azusa Yamazaki, Eriko Takashima, Jun-Woo Park, Kazuhide Ueno, Shiro Seki, and Nobuyuki Serizawa. Solvate ionic liquid electrolyte for li-s batteries. *Journal of the Electrochemical Society*, 160(8):A1304–A1310, January 2013.

[44] Jiangfeng Qian, Wesley A Henderson, Wu Xu, Priyanka Bhattacharya, Mark Engelhard, Oleg Borodin, and Ji-Guang Zhang. High rate and stable cycling of lithium metal anode. *Nature Communications*, 6(1):6362, 2015.

[45] Yuki Yamada, Kenji Usui, Ching Hua Chiang, Keisuke Kikuchi, Keizo Furukawa, and Atsuo Yamada. General observation of lithium intercalation into graphite in ethylene-carbonate-free superconcentrated electrolytes. *ACS Applied Materials & Interfaces*, 6(14):10892–10899, 2014. PMID: 24670260.

[46] Luis Aguilera, Shizhao Xiong, Johan Scheers, and Aleksandar Matic. A structural study of LiTFSI–tetraglyme mixtures: From diluted solutions to solvated ionic liquids. *Journal of Molecular Liquids*, 210:238–242, 2015.

[47] Rachid Amine, Jianzhao Liu, Ilona Acznik, Tian Sheng, Katarzyna Lota, Hui Sun, Cheng-Jun Sun, Krzysztof Fic, Xiaobing Zuo, Yang Ren, Deia Abd EI-Hady, Wael Alshitari, Abdullah S Al-Bogami, Zonghai Chen, Khalil Amine, and Gui-Liang Xu. Regulating the Hidden Solvation-Ion-Exchange in Concentrated Electrolytes for Stable and Safe Lithium Metal Batteries. *Advanced Energy Materials*, n/a(n/a):2000901, jun 2020.

[48] Daniel M Seo, Oleg Borodin, Daniel Balogh, Michael O'Connell, Quang Ly, Sang-Don Han, Stefano Passerini, and Wesley A Henderson. Electrolyte Solvation and Ionic Association III. Acetonitrile-Lithium Salt Mixtures–Transport Properties. *Journal of The Electrochemical Society*, 160(8):A1061–A1070, 2013.

[49] Gustav Åvall and Patrik Johansson. A novel approach to ligand-exchange rates applied to lithium-ion battery and sodium-ion battery electrolytes. *The Journal of chemical physics*, 152(23):234104, jun 2020.

[50] Kaoru Dokko, Daiki Watanabe, Yosuke Ugata, Morgan L Thomas, Seiji Tsuzuki, Wataru Shinoda, Kei Hashimoto, Kazuhide Ueno, Yasuhiro Umebayashi, and Masayoshi Watanabe. Direct Evidence for Li Ion Hopping Conduction in Highly Concentrated Sulfolane-Based Liquid Electrolytes. *The Journal of Physical Chemistry B*, 122(47):10736–10745, nov 2018.

[51] Chi-Cheung Su, Meinan He, Rachid Amine, and Khalil Amine. A selection rule for hydrofluoroether electrolyte cosolvent: Establishing a linear free-energy relationship in lithium–sulfur batteries. *Angewandte Chemie International Edition*, 58(31):10591–10595, 2019.

[52] Lei Qin, Neng Xiao, Jingfeng Zheng, Yu Lei, Dengyun Zhai, and Yiying Wu. Localized high-concentration electrolytes boost potassium storage in high-loading graphite. *Advanced Energy Materials*, 9(44):1902618, 2019.

[53] Jun-Fan Ding, Rui Xu, Nan Yao, Xiang Chen, Ye Xiao, Yu-Xing Yao, Chong Yan, Jin Xie, and Jia-Qi Huang. Non-solvating and low-dielectricity cosolvent for anion-derived solid electrolyte interphases in lithium metal batteries. *Angewandte Chemie International Edition*, 60(20):11442–11447, 2021.

[54] Hai Lu, Yan Yuan, Zhenzhong Hou, Yanqing Lai, Kai Zhang, and Yexiang Liu. Solvate ionic liquid electrolyte with 1,1,2,2-tetrafluoroethyl 2,2,2-trifluoroethyl ether as a support solvent for advanced lithium–sulfur batteries. *RSC Adv.*, 6:18186–18190, 2016.

[55] Shaohua Fang, Long Qu, Dong Luo, Shumin Shen, Li Yang, and Shin-ichi Hirano. Novel mixtures of ether-functionalized ionic liquids and non-flammable methylperfluorobutylether as safe electrolytes for lithium metal batteries. *RSC Adv.*, 5:33897–33904, 2015.

[56] Xu Liu, Maider Zarrabeitia, Alessandro Mariani, Xinpei Gao, Hanno Maria Schütz, Shan Fang, Thomas Bizien, Giuseppe Antonio Elia, and Stefano Passerini. Enhanced li+ transport in ionic liquid-based electrolytes aided by fluorinated ethers for highly efficient lithium metal batteries with improved rate capability. *Small Methods*, 5(7):2100168, 2021.

[57] Zhicheng Wang, Fengrui Zhang, Yiyang Sun, Lei Zheng, Yanbin Shen, Daosong Fu, Wanfei Li, Anran Pan, Lei Wang, Jingjing Xu, Jianchen Hu, and Xiaodong Wu. Intrinsically nonflammable ionic liquid-based localized highly concentrated electrolytes enable high-performance li-metal batteries. *Advanced Energy Materials*, 11(17):2003752, 2021.

[58] Hai Lu, Zhen Chen, Huiling Du, Kai Zhang, Jinlei Wang, Zhenzhong Hou, and Jing Fang. The enhanced performance of lithium sulfur battery with ionic liquid-based electrolyte mixed with fluorinated ether. *Ionics*, 25(6):2685–2691, 2019.

[59] Saul Perez Beltran, Xia Cao, Ji-Guang Zhang, and Perla B Balbuena. Localized High Concentration Electrolytes for High Voltage Lithium–Metal Batteries: Correlation between the Electrolyte Composition and Its Reductive/Oxidative Stability. *Chemistry of Materials*, 32(14):5973–5984, jul 2020.

[60] G B Appetecchi, M Montanino, and S Passerini. Ionic Liquid-Based Electrolytes for High Energy, Safer Lithium Batteries. In *Ionic Liquids: Science and Applications*, volume 1117 of *ACS Symposium Series*, pages 4–67. American Chemical Society, jan 2012.

[61] K. Ghandi. A Review of Ionic Liquids, Their Limits and Applications. *Green and Sustainable Chemistry*, 4(1):44–53, 2014.

[62] Erlendur Jónsson. Ionic liquids as electrolytes for energy storage applications – A modelling perspective. *Energy Storage Materials*, 25:827–835, 2020.

[63] Tamar L. Greaves and Calum J. Drummond. Protic ionic liquids: Evolving structure–property relationships and expanding applications. *Chemical Reviews*, 115(20):11379–11448, 2015. PMID: 26426209.

[64] Apurba Ray and Bilge Saruhan. Application of ionic liquids for batteries and supercapacitors. *Materials*, 14(11), 2021.

[65] Daniel Rauber, Andreas Hofmann, Frederik Philippi, Christopher W. M. Kay, Tatiana Zinkevich, Thomas Hanemann, and Rolf Hempelmann. Structure-property relation of trimethyl ammonium ionic liquids for battery applications. *Applied Sciences*, 11(12), 2021.

[66] Anna Martinelli, Aleksandar Matic, Per Jacobsson, Lars Bo, Alessandra Fernicola, and Bruno Scrosati. Phase Behavior and Ionic Conductivity in Lithium Bis (trifluoromethanesulfonyl) imide-Doped Ionic Liquids of the Pyrrolidinium Cation and Bis (trifluoromethanesulfonyl) imide Anion. *Solutions*, pages 11247–11251, 2009.

[67] Gaetan M. A. Girard, Matthias Hilder, Nicolas Dupre, Dominique Guyomard, Donato Nucciarone, Kristina Whitbread, Serguei Zavorine, Michael Moser, Maria Forsyth, Douglas R. MacFarlane, and Patrick C. Howlett. Spectroscopic characterization of the sei layer formed on lithium metal electrodes in phosphonium bis(fluorosulfonyl)imide ionic liquid electrolytes. *ACS Applied Materials & Interfaces*, 10(7):6719–6729, 2018. PMID: 29377667.

[68] Travis Mackoy, Nicholas A Mauro, and Ralph A Wheeler. Temperature Dependence of Static Structure Factor Peak Intensities for a Pyrrolidinium-Based Ionic Liquid. *The Journal of Physical Chemistry B*, 123(7):1672–1678, feb 2019.

[69] Luis Aguilera, Johannes Völkner, Ana Labrador, and Aleksandar Matic. The effect of lithium salt doping on the nanostructure of ionic liquids. *Phys. Chem. Chem. Phys.*, 17(40):27082–27087, 2015.

[70] Alessandro Triolo, Olga Russina, Hans-Jurgen Bleif, and Emanuela Di Cola. Nanoscale Segregation in Room Temperature Ionic Liquids. *The Journal of Physical Chemistry B*, 111(18):4641–4644, may 2007.

[71] Jagath Pitawala, Anna Martinelli, Patrik Johansson, Per Jacobsson, and Aleksandar Matic. Coordination and interactions in a Li-salt doped ionic liquid. *Journal of Non-Crystalline Solids*, 407:318–323, 2015.

[72] Jean-Claude Lassègues, Joseph Grondin, Christian Aupetit, and Patrik Johansson. Spectroscopic identification of the lithium ion transporting species in litfsi-doped ionic liquids. *The Journal of Physical Chemistry A*, 113(1):305–314, 2009. PMID: 19072213.

[73] Anita Yadav, Abhirup Guha, Ashish Pandey, Mahi Pal, Shruti Trivedi, and Siddharth Pandey. Densities and dynamic viscosities of ionic liquids having 1-butyl-3-methylimidazolium cation with different anions and bis(trifluoromethylsulfonyl)imide anion with different cations in the temperature range (283.15 to 363.15)k. *The Journal of Chemical Thermodynamics*, 116:67–75, 2018.

[74] Faiz Ullah Shah, Oleg I. Gnezdilov, and Andrei Filippov. Ion dynamics in halogen-free phosphonium bis(salicylato)borate ionic liquid electrolytes for lithium-ion batteries. *Phys. Chem. Chem. Phys.*, 19:16721–16730, 2017.

[75] Giuseppe Antonio Elia, Ulderico Ulissi, Sangsik Jeong, Stefano Passerini, and Jusef Hassoun. Exceptional long-life performance of lithium-ion batteries using ionic liquid-based electrolytes. *Energy Environ. Sci.*, 9:3210–3220, 2016.

[76] Xinpei Gao, Fanglin Wu, Alessandro Mariani, and Stefano Passerini. Concentrated Ionic-Liquid-Based Electrolytes for High-Voltage Lithium Batteries with Improved Performance at Room Temperature. *ChemSusChem*, 12(18):4185–4193, 2019.

[77] Jagath Pitawala, Jae Kwang Kim, Per Jacobsson, Victor Koch, Fausto Croce, and Aleksandar Matic. Phase behaviour, transport properties, and interactions in Li-salt doped ionic liquids. *Faraday Discussions*, 154:71–80, 2012.

[78] Valérie Mazan and Maria Boltoeva. Insight into the ionic interactions in neat ionic liquids by Diffusion Ordered Spectroscopy Nuclear Magnetic Resonance. *Journal of Molecular Liquids*, 240:74–79, 2017.

[79] C J F Solano, S Jeremias, E Paillard, D Beljonne, and R Lazzaroni. A joint theoretical/experimental study of the structure, dynamics, and Li+ transport in bis([tri]fluoro[methane]sulfonyl)imide [T]FSI-based ionic liquids. *The Journal of Chemical Physics*, 139(3):34502, jul 2013.

[80] Maiko Kofu, Michihiro Nagao, Takeshi Ueki, Yuzo Kitazawa, Yutaro Nakamura, Syota Sawamura, Masayoshi Watanabe, and Osamu Yamamuro. Heterogeneous Slow Dynamics of Imidazolium-Based Ionic Liquids Studied by Neutron Spin Echo. *The Journal of Physical Chemistry B*, 117(9):2773–2781, mar 2013.

[81] Maiko Kofu, Madhusudan Tyagi, Yasuhiro Inamura, Kyoko Miyazaki, and Osamu Yamamuro. Quasielastic neutron scattering studies on glass-forming ionic liquids with imidazolium cations. *The Journal of Chemical Physics*, 143(23):234502, 2015.

[82] Fumiya Nemoto, Maiko Kofu, Michihiro Nagao, Kazuki Ohishi, Shin-ichi Takata, Jun-ichi Suzuki, Takeshi Yamada, Kaoru Shibata, Takeshi Ueki, Yuzo Kitazawa, Masayoshi Watanabe, and Osamu Yamamuro. Neutron scattering studies on short- and long-range layer structures and related dynamics in imidazolium-based ionic liquids. *The Journal of Chemical Physics*, 149(5):54502, 2018.

[83] Miguel A González, Bachir Aoun, David L Price, Zunbeltz Izaola, Margarita Russina, Jacques Ollivier, and Marie-Louise Saboungi. Molecular dynamics in 1-alkyl-3-methylimidazolium bromide ionic liquids: A reanalysis of quasielastic neutron scattering results. *AIP Conference Proceedings*, 1969(1):20002, 2018.

[84] Filippo Ferdeghini, Quentin Berrod, Jean-Marc Zanotti, Patrick Judeinstein, Victoria García Sakai, Orsolya Czakkel, Peter Fouquet, and Doru Constantin. Nanostructuration of ionic liquids: impact on the cation mobility. A multi-scale study. *Nanoscale*, 9(5):1901–1908, 2017.

[85] N Yaghini, L Nordstierna, and A Martinelli. Effect of water on the transport properties of protic and aprotic imidazolium ionic liquids – an analysis of self-diffusivity, conductivity, and proton exchange mechanism. *Physical Chemistry Chemical Physics*, 16(20):9266–9275, 2014.

[86] Timo Stettner, Sascha Gehrke, Promit Ray, Barbara Kirchner, and Andrea Balducci. Water in Protic Ionic Liquids: Properties and Use of a New Class of Electrolytes for Energy-Storage Devices. *ChemSusChem*, 12(16):3827–3836, aug 2019.

[87] Oleg Borodin, David L. Price, Bachir Aoun, Miguel A. González, Justin B. Hooper, Maiko Kofu, Shinji Kohara, Osamu Yamamuro, and Marie-Louise Saboungi. Effect of water on the structure of a prototype ionic liquid. *Phys. Chem. Chem. Phys.*, 18:23474–23481, 2016.

[88] David L Price, Oleg Borodin, Miguel A González, Maiko Kofu, Kaoru Shibata, Takeshi Yamada, Osamu Yamamuro, and Marie-Louise Saboungi. Relaxation in a Prototype Ionic Liquid: Influence of Water on the Dynamics. *The Journal of Physical Chemistry Letters*, 8(4):715–719, feb 2017.

[89] M. D. Ruiz-Martín, N. Qureshi, M. A. González, J. Ollivier, B. Frick, and B. Farago. Influence of water on the microscopic dynamics of 1-butyl-3-methylimidazolium tetrafluoroborate studied by means of quasielastic neutron scattering. *The Journal of Chemical Physics*, 156(8):084505, 2022.

[90] Jonathan G. Huddleston, Ann E. Visser, W. Matthew Reichert, Heather D. Willauer, Grant A. Broker, and Robin D. Rogers. Characterization and comparison of hydrophilic and hydrophobic room temperature ionic liquids incorporating the imidazolium cation. *Green Chem.*, 3:156–164, 2001.

[91] Jingsi Gao and Norman J Wagner. Water Nanocluster Formation in the Ionic Liquid 1-Butyl-3-methylimidazolium Tetrafluoroborate ([C4mim][BF4]) – D2O Mixtures. *Langmuir*, 32(20):5078–5084, may 2016.

[92] Sascha Gehrke, Promit Ray, Timo Stettner, Andrea Balducci, and Barbara Kirchner. Water in protic ionic liquid electrolytes: From solvent separated ion pairs to water clusters. *ChemSusChem*, 14(16):3315–3324, 2021.

[93] Andreas Schönhals Friedrich Kremer. *Broadband Dielectric Spectroscopy*. Springer-Verlag Berlin Heidelberg, 1 edition, 2003.

[94] Sverre Grimnes and Ørjan G Martinsen. Chapter 3 - dielectrics. In Sverre Grimnes and Ørjan G Martinsen, editors, *Bioimpedance and Bioelectricity Basics (Third Edition)*, pages 37 – 75. Academic Press, Oxford, third edition, 2015.

[95] Lauren Boldon, Fallon Laliberte, and Li Liu. Review of the fundamental theories behind small angle X-ray scattering, molecular dynamics simulations, and relevant integrated application. *Nano reviews*, 6:25661, feb 2015.

[96] Philip Willmott. *An Introduction to Synchrotron Radiation : Techniques and Applications*. John Wiley & Sons, Incorporated, 2019.

[97] Kinematical scattering I: non-crystalline materials, mar 2011.

[98] J. Als-Nielsen. *Diffraction, refraction and absorption of X-rays and neutrons: A comparative exposition*, chapter 1. Springer-Verlag Berlin Heidelberg, 1994.

[99] Peter Larkin. *Infrared and Raman Spectroscopy : Principles and Spectral Interpretation*. Elsevier, Saint Louis, UNITED STATES, 2011.

[100] Quasielastic Neutron Scattering: An Advanced Technique for Studying the Relaxation Processes in Condensed Matter, 2016.

[101] G L Squires. *Introduction to the Theory of Thermal Neutron Scattering*. Cambridge University Press, Cambridge, 3 edition, 2012.

[102] Jacques Ollivier and Hannu Mutka. In5 cold neutron time-of-flight spectrometer, prepared to tackle single crystal spectroscopy. *Journal of the Physical Society of Japan*, 80(Suppl.B):SB003, 2011.

[103] S. Janßen, J. Mesot, L. Holitzner, A. Furrer, and R. Hempelmann. Focus: a hybrid tof-spectrometer at sinq. *Physica B: Condensed Matter*, 234-236:1174–1176, 1997. Proceedings of the First European Conference on Neutron Scattering.

[104] B. Frick, M. Appel, T. Seydel, L. van Eijck, and D. Bazzoli. Backscattering spectrometer in16b, institute laue-langevin, 2017. Last accessed 1 June 2022.

[105] F. Mezei. *Neutron Spin Echo: Proceedings of a Laue-Langevin Institut Workshop*. Springer-Verlag, Grenoble, 1 edition, 1980.

[106] Mark T. F. Telling. *A practical guide to quasi-elastic neutron scattering*. Royal Society of Chemistry, 2020.

[107] Tatsiana Burankova, Juan F Mora Cardozo, Daniel Rauber, Andrew Wildes, and Jan P Embs. Linking Structure to Dynamics in Protic Ionic Liquids: A Neutron Scattering Study of Correlated and Single-Particle Motions. *Scientific Reports*, 8(1):16400, 2018.

[108] D. Richard, M. Ferrand, and G. J. Kearley. Analysis and visualisation of neutron-scattering data. *Journal of Neutron Research*, 4(1-4):33–39, 1996.

[109] Richard Tumanjong Azuah, Larry R Kneller, Yiming Qiu, Philip L W Tregenna-Piggott, Craig M Brown, John R D Copley, and Robert M Dimeo. DAVE: A Comprehensive Software Suite for the Reduction, Visualization, and Analysis of Low Energy Neutron Spectroscopic Data. *Journal of research of the National Institute of Standards and Technology*, 114(6):341–358, dec 2009.

[110] O. Arnold, J.C. Bilheux, J.M. Borreguero, A. Buts, S.I. Campbell, L. Chapon, M. Doucet, N. Draper, R. Ferraz Leal, M.A. Gigg, V.E. Lynch, A. Markvardsen, D.J. Mikkelson, R.L. Mikkelson, R. Miller, K. Palmen, P. Parker, G. Passos, T.G. Perring, P.F. Peterson, S. Ren, M.A. Reuter, A.T. Savici, J.W. Taylor, R.J. Taylor, R. Tolchenov, W. Zhou, and J. Zikovsky. Mantid—data analysis and visualization package for neutron scattering and μ sr experiments. *Nuclear Instruments and Methods in Physics Research Section A: Accelerators, Spectrometers, Detectors and Associated Equipment*, 764:156–166, 2014.

[111] Quentin Berrod, Karine Lagrené, Jacques Ollivier, and Jean-Marc Zanotti. Inelastic and quasi-elastic neutron scattering. application to soft-matter. *EPJ Web of Conferences*, 188(05001), 2018.

[112] Adolph Fick. On liquid diffusion. *Journal of Membrane Science*, 100(1):33–38, 1995. The early history of membrane science selected papers celebrating vol. 100.

[113] Marc Bée. *Quasielastic neutron scattering: principles and applications in solid state chemistry, biology and materials science*. IOP Publishing Ltd, Bristol, 1 edition, 1988.

[114] Peter L. Hall and D.K. Ross. Incoherent neutron scattering functions for random jump diffusion in bounded and infinite media. *Molecular Physics*, 42(3):673–682, 1981.

[115] J Teixeira, M.-C. Bellissent-Funel, S H Chen, and A J Dianoux. Experimental determination of the nature of diffusive motions of water molecules at low temperatures. *Physical Review A*, 31(3):1913–1917, mar 1985.

[116] Nicholas A. Mauro Allison M. Fleshman. Temperature-dependent structure and transport of ionic liquids with short-and intermediate-chain length pyrrolidinium cations. *Journal of Molecular Liquids*, 279:23–31, 2019.

[117] Alessandro Triolo, Andrea Mandanici, Olga Russina, Virginia Rodriguez-Mora, Maria Cutroni, Christopher Hardacre, Mark Nieuwenhuyzen, Hans-Jurgen Bleif, Lukas Keller, and Miguel Angel Ramos. Thermodynamics, Structure, and Dynamics in Room Temperature Ionic Liquids: The Case of 1-Butyl-3-methyl Imidazolium Hexafluorophosphate ([bmim][PF6]). *The Journal of Physical Chemistry B*, 110(42):21357–21364, 2006.

[118] Kartik Pilar, Victor Balédent, Mehdi Zeghal, Patrick Judeinstein, Sangsik Jeong, Stefano Passerini, and Steve Greenbaum. Communication: Investigation of ion aggregation in ionic liquids and their solutions with lithium salt under high pressure. *The Journal of Chemical Physics*, 148(3):31102, 2018.

[119] Henriette Wase Hansen, Filippa Lundin, Karolina Adrjanowicz, Bernhard Frick, Aleksandar Matic, and Kristine Niss. Density scaling of structure and dynamics of an ionic liquid. *Physical Chemistry Chemical Physics*, 22:14169–14176, 2020.

[120] Patrik Johansson, Leif Erik Fast, Aleksandar Matic, Giovanni B. Appetecchi, and Stefano Passerini. The conductivity of pyrrolidinium and sulfonylimide-based ionic liquids: A combined experimental and computational study. *Journal of Power Sources*, 195(7):2074–2076, 2010.

[121] Maiko Kofu, Antonio Faraone, Madhusudan Tyagi, Michihiro Nagao, and Osamu Yamamuro. Two inherent crossovers of the diffusion process in glass-forming liquids. *Phys. Rev. E*, 98:042601, Oct 2018.